Chaos, Solitons and Fractals 199 (2025) 116855

Contents lists available at ScienceDirect

Chaos, Solitons and Fractals

journal homepage: www.elsevier.com/locate/chaos

Ghost hammering in a randomly excited nonlinear dynamical system

Francesco Pellicano *, Antonio Zippo

Department of Engineering "Enzo Ferrari", Centre InterMech MoRe, University of Modena and Reggio Emilia, Modena, Italy

ARTICLE INFO

Keywords:
Random vibration
Shells
Nonlinear dynamics
Stochastic resonance
Complexity

ABSTRACT

Random phenomena are widespread across disciplines such as Engineering, Physics, Geophysics, and Medicine, often arising from the inherent variability of natural systems. In Structural Mechanics, sources of randomness include environmental forces like wind, seismic activity, and manufacturing tolerances, which can induce vibrations with unpredictable features. While linear methods have traditionally been used to analyse such vibrations, they often fail to capture the complex behaviour that emerges in nonlinear systems.

This study investigates the dynamic response of a circular cylindrical shell subjected to high-energy, narrowband random seismic excitation. Experimental observations revealed the occurrence of irregular, high-amplitude spikes in the system's response, events unpredictable and incomprehensible by using linear models. These phenomena bear a strong resemblance to Extreme Events (EE), Stochastic Resonance (SR), Bursting Behaviour (BB), and Spiking Oscillations (SO) observed in fields like Neuroscience, Optics, and Electronics, but rarely documented in Solid Mechanics. The observed spikes, termed "Ghost Hammering (GH)," appear as transient oscillations at the system's natural frequencies, resembling sudden impacts despite the absence of external impulses. Their behaviour suggests strong nonlinear interactions triggered by random excitation. Models used in neuroscience and nonlinear physics, such as van der Pol, FitzHugh–Nagumo, and Langevin systems, offer promising frameworks for interpreting these phenomena. The paper details the experimental setup and standard modal analysis of the shell, followed by a focused discussion of the extreme events observed. These findings highlight the need to expand the application of stochastic nonlinear models to structural systems, offering new perspectives on how randomness can drive unexpected behaviours in mechanical structures.

1. Introduction

Random phenomena are common in several scientific fields, including Engineering, Physics, Geophysics, and Medicine. Such non-deterministic occurrences often stem from the inherent variability in natural processes. For example, external forces such as wind, seismic activity, or ocean waves can generate random vibrations; buildings might experience random vibrations due to wind gusts or traffic; components in machines, vehicles, or engines can generate random vibrations because of the inherent randomness in manufacturing processes, wear, and component tolerances; in electronics and communications, random oscillations can be induced by acoustic noise or electromagnetic interference, leading to distortion in sensitive devices. Physics deals with random phenomena at both microscopic and macroscopic scales; for example, quantum mechanics is built on the concept of probability; randomness is evident in thermodynamics and statistical mechanics. In geophysics, randomness plays a significant role in natural processes like seismic activity, volcanic eruptions, and weather patterns. Earthquakes, for instance, occur as a result of unpredictable shifts in tectonic plates, and while some patterns can be analysed, the exact timing and magnitude of an earthquake are inherently uncertain. Medicine frequently faces with random phenomena, especially in areas related to human biology, disease spread, and treatment efficacy; for example, neurons do not always respond in a perfectly predictable manner to inputs; their electrical activity is subject to random fluctuations due to various factors such as ion channel noise, synaptic variability, and intrinsic membrane properties. These fluctuations can influence the timing and frequency of action potentials (spikes), leading to variability in neural responses even when stimuli are constant. This variability is often described using stochastic models of neural activity.

The present study is focused on complex phenomena appearing when a high-energy seismic random vibration excites a circular cylindrical shell. Random vibrations are traditionally analysed using linear models and methods [1] such as autocorrelation functions, auto and cross

* Corresponding author.
E-mail addresses: francesco.pellicano@unimore.it (F. Pellicano), antonio.zippo@unimore.it (A. Zippo).

https://doi.org/10.1016/j.chaos.2025.116855
Received 24 May 2025; Received in revised form 24 June 2025; Accepted 4 July 2025
Available online 18 July 2025

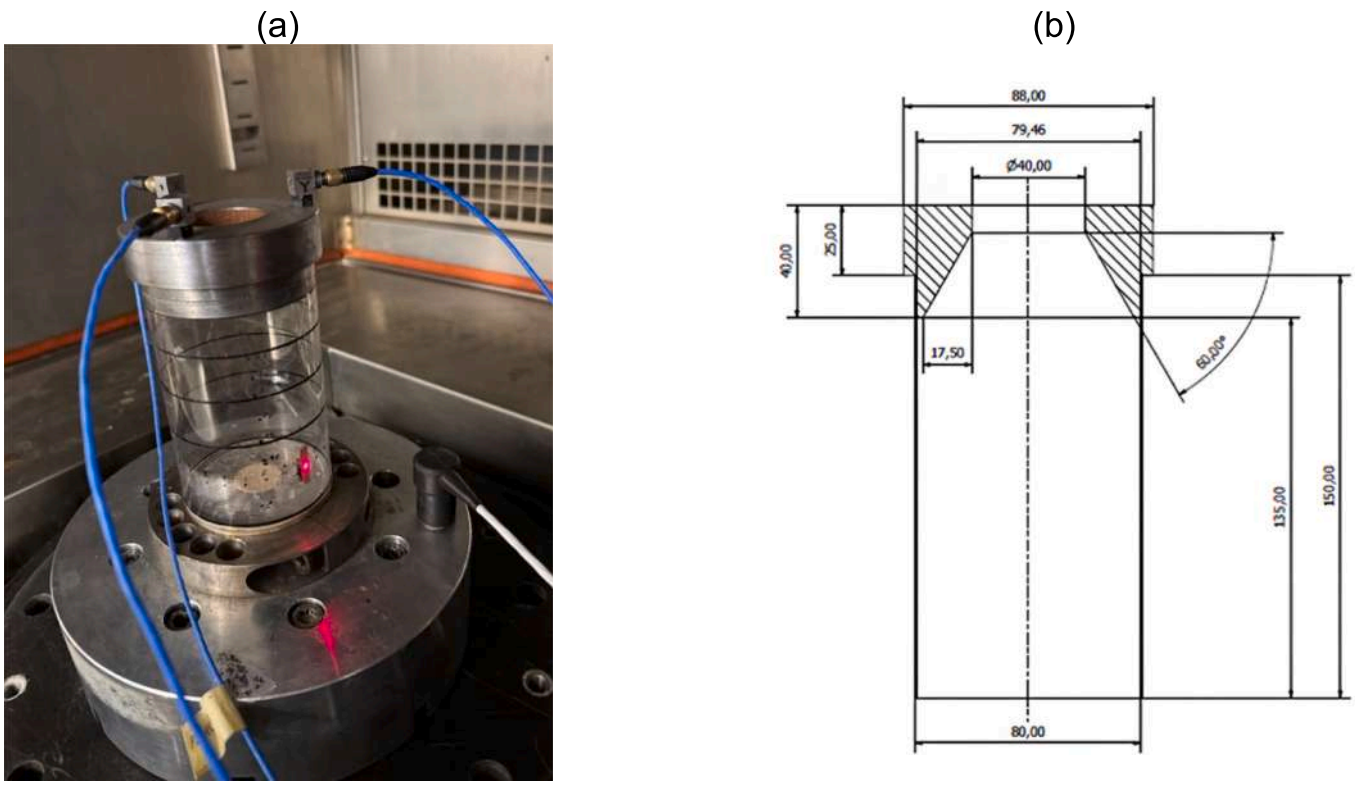

Fig. 1. (a) Instrumented test specimen shell, and (b) shell-disk assembly technical drawing.

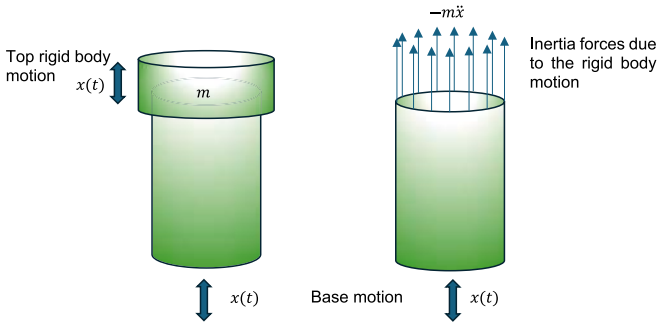

Fig. 2. Inertia forces due to the seismic excitation.

spectra, and frequency response functions; however, such methods fail when the dynamic systems exhibit nonlinearities. In Ref. [2] an early theory on modelling in nonlinear random vibrations by Markov processes was presented. More recently, Roberts and Spanos [3] published a book focused on techniques suitable for analysing nonlinear vibrations through statistical linearization; Spanos and Donley [4] proposed a statistical approach for the analysis of nonlinear systems.

Although the aforementioned theories and methods are extremely effective for the most of problems encountered in engineering vibration problems, some phenomena observed in strongly nonlinear dynamical systems must be analysed on different bases. In particular, in the present work, we present experimental evidence of some phenomena similar but not identical to those that in the literature have been named Extreme Events (EE), Stochastic Resonances (SR), Bursting Behaviours (BB), and Spiking Oscillations (SO). In the following, we describe the literature focused on such phenomena, which have been observed in contexts like Neurology, Microelectronics, and Geophysics; note that examples in Solid Mechanics are almost absent.

One of the first and most important papers, published in 1981, that explained the mechanism of SR is due to Benzi et al. [5]. The question they faced was: "What causes the nearly periodic recurrence of the primary ice age cycle approximately every 100,000 years?"; the Earth's orbit eccentricity presents an eccentricity with a period of 100,000 years; however, current theories suggest that this variation alone is not significant enough to trigger such drastic climate changes. Benzi et al. proposed a cooperative interaction between the small periodic oscillations in orbital eccentricity and random fluctuations resulting from short-term climate variability; they considered a Langevin equation driven by a Wiener process to estimate the probability of escape from the basin of attraction, they also stated: "We believe that this mechanism can also be important for those systems showing Hopf bifurcation and stochastic forcing, as recently described by Graham (1980)" [6].

Gammaitoni et al. [7] published in 1998 a comprehensive review on SR. This paper discusses theory, key characteristics, and applications in optics, solid-state devices, and neurophysiology. It also explores quantum properties, spatial aspects, chaotic maps, and future research directions.

Gao et al. [8] studied the effect of noise on a logistic map, showing that noise can induce chaos. Noise below a certain range can't induce chaos; within such a range, it preserves adjacent chaotic states, and weak noise causes super-diffusive behaviour beyond Brownian motion.

In 2002, Feng and Hu [9] analysed the stability of a beam subject to narrowband random parametric excitation using Kane's method. Young and Gaud [10] analysed the stability of spinning beams with pre-twist under axial stochastic forces, using a stochastic averaging method.

Using the multiple-scale perturbation method Li et al. [11] 2004 analysed the principal resonance of a Duffing-Mathieu equation, where the parametric forcing was the classical sinusoidal function perturbed with a Wiener process, the nonlinearity was of a cubic type, the authors claimed that the random perturbation level influences the stability of the trivial steady state.

Muratova et al. [12] studied the escape from a slow manifold due to the presence of low noise, which can induce excursions of the system to a deterministic state, they named the phenomenon: "Self Induced Stochastic Resonance"; this is characterized by a series of spikes in the time

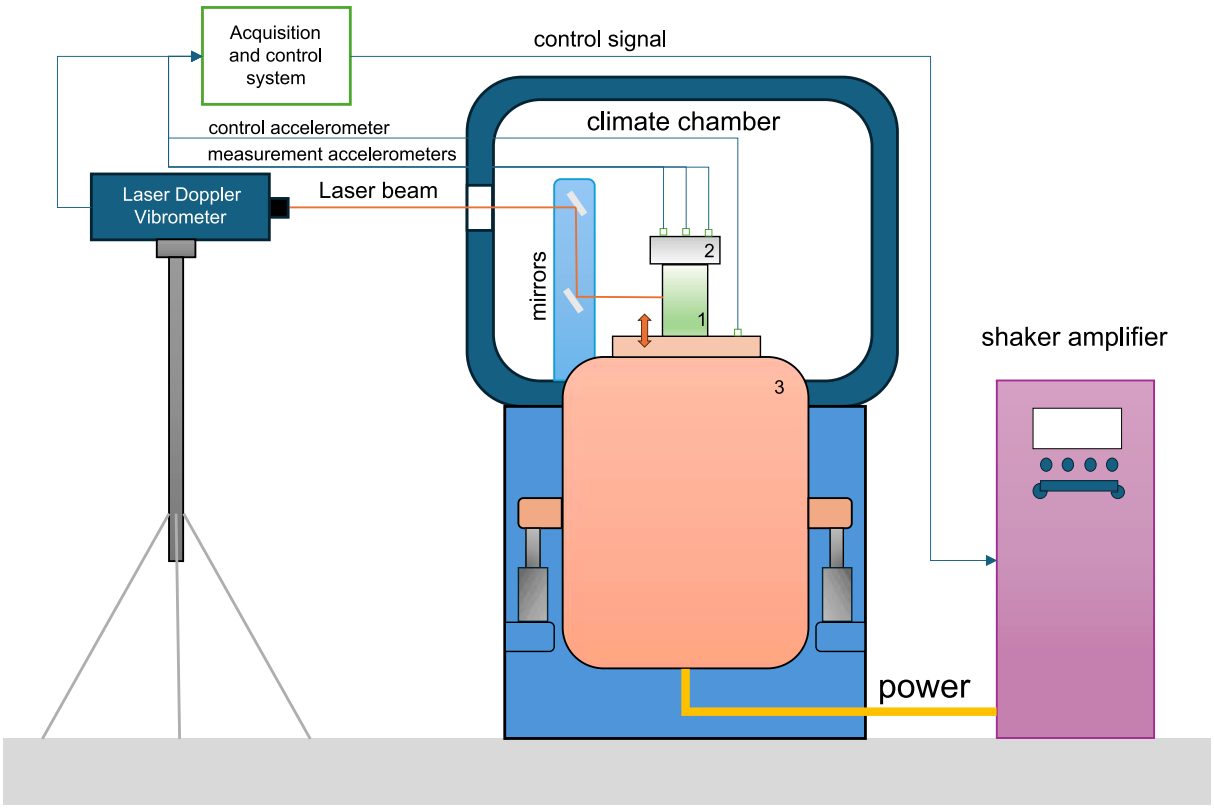

Fig. 3. Experimental setup. 1) Specimen, 2) inertial mass, 3) shaker.

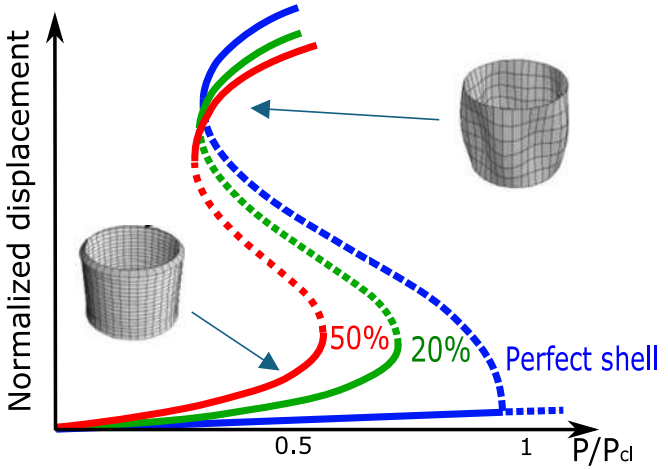

Fig. 4. Qualitative pre- and post-buckling paths of a circular cylindrical shell. Perfect shell: blue line; 20 % and 50 % imperfection with respect to the thickness, green and red lines. Continuous line: stable branch; dashed line: unstable branch. (For interpretation of the references to colour in this figure legend, the reader is referred to the web version of this article.)

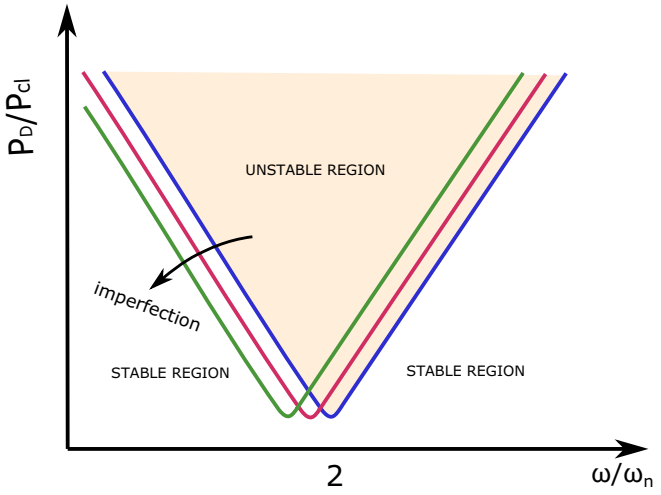

Fig. 5. Qualitative dynamic scenario of dynamic instability under parametric periodic excitation [54].

behaviour of the state variables.

Dobson et al. [13] used the framework of self-organized criticality to explain the mechanism of cascading failure in power grids. The occurrence of oceanic rogue waves was explored in [14] through measurements of the output intensity in an optically injected semiconductor laser setup. Additionally, a theoretical model of the laser was considered to better understand the mechanism behind the generation of rare pulses.

Brouwers [15] studied a Mathieu-type equation with purely Gaussian process excitation, used for simulating the dynamics of a floating offshore platform.

Tantet et al. [16] provided a general theoretical framework to analyse a stochastic Hopf bifurcation based on the statistical characterization of the stability of nonlinear oscillators under the influence of noise.

Zhu et al. [17] applied a path integration method to analyse the stochastic response of a marine riser with parametric and direct Gaussian excitation. They compared the approach with equivalent linearization, and they mainly focused their attention on the probability density of the response.

In 2020, Ramakrishnan and Edlund [18] studied the stochastic

Table 1
Natural frequencies, damping ratios, and identified mode type at room temperature, 28 °C.

Mode number	Mode type (m,n) m = longitudinal half-waves n = nodal diameters	Natural frequency Hz	Damping ratio
1	First bending	68.27	1.60
2	Torsional bending	68.92	0.69
3	Torsional mode	193.38	1.02
4	(1,0) first axisymmetric	259.96	0.66
5	(1,1) second beam mode	413.82	0.93
6	(1,1) second beam mode	416.69	1.04
7	(1,5)	794.94	0.96
8	(1,5)	814.46	0.96
9	(1,6)	856.76	1.75
10	(1,6)	932.41	1.07
11	(1,4)	940.19	1.04
12	(1,7)	1050.4	1.04
13	(1,7)	1063.9	1.06
14	(1,3)	1275.4	1.15
15	(2,6)	1397.6	1.22
16	(2,7)	1425.3	1.1
17	(2,7)	1445.4	1.17

vibrations of a piezoelectric harvester, they analytically obtained the stability bounds of noise intensity in the nonlinear, non-Brownian, and superdiffusive process regimes.

Kuptsova [19] published in 2020 a theoretical analysis on the effect of random noise perturbation on the dynamics of a nonlinear oscillator, finding the first approximations of the expectation and the dispersion function of the solution.

In 2021, Qian and Chen [20] investigated the stochastic bifurcation of a nonsmooth vibro-impact system and estimated the probability density function, they found that the stability of the system is strictly correlated with the noise level. Wang et al. [21] analysed the resonance of a system of coupled Duffing oscillators with active passive hybrid coupled control, their study shows rich dynamics with double jumps and bifurcations (B-tipping). Yang et al. [22] used the stochastic average method to obtain the analytical form of probability density functions of a galloping-based piezoelectric harvester of a buoy platform.

In Ref. [23] it was shown that noise can induce limit cycles, caused by self-induced stochastic resonance, in a non-symmetric multi-well dynamical system, inducing spikes in the time response; the Wentzel-Kramers-Brillouin approximation was used for estimating the time interval of limit cycles.

In 2022, Bashkirtseva and Slepukhina [24] studied random perturbations of a bi-stable cold-flame combustion of hydrocarbon mixtures, showing transitions between stable equilibria and limit cycles, leading to complex stochastic mixed-mode oscillations. InterSpike Interval statistics of these regimes were analysed, and the phenomenon of "anti-coherence resonance" was discussed.

Ramakrishnan and Singh [25] compared the Itô and Stratonovich interpretation of a stochastic differential equation, underlining that the two approaches give different results in evaluating the stochastic integral.

Generalized stochastic resonances were studied by Zhang et al. [26]. In such a study, this kind of phenomenon was observed in complex networks, where synchronizations, instabilities, and resonances can take place.

1.1. Neurological models

The field where the concept of SR finds the largest application is Neurology, in particular in studying brain and nerve electric signals and response to stimuli.

Fitzhugh [27] published in 1961 one of the first studies focused on theoretical models of nerve membranes; the paper explains how trains of impulses occur in the Hodgkin-Huxley equations. Recently, Baltanáis and Casado [28] analysed the FitzHugh-Nagumo (FHN) neuron model subjected to a very narrow band noise, showing that bursts in the response are characterized by a timing sequence period corresponding to the central frequency of the noise.

Muratov and Vanden-Eijnden [29] considered the Morris-Lecar model, which is a stochastic differential equation set used for studying type-II neurons. They developed an asymptotic approach for analysing limit cycles and coherence resonance limits induced by stochastic resonance.

Faisal et al. [30] published in 2008 a review paper focused on the analysis of noise in nervous systems; they examined noise's impact on neuronal networks, the nervous system's countermeasures, and its potential benefits.

In 2009, Channell et al. [31] studied the variability of spikes and bursts of neurons, considering the influence of noise. They reported that, even though experimental studies show that the bursting duration variability appears as a rule rather than an exception, the models prove that the bursting interneuron dynamics are extremely sensitive to noise.

In Ref. [66], Ostojic studied the InterSpike Interval (ISI) distributions of neurons excited by oscillating inputs, with a focus on the stochastic dynamics of the membrane potential. The study found that, regardless of the specific neuronal model, when the mean input current is below the threshold, the membrane potential exhibits stochastic behaviour and the threshold-crossing times are broadly distributed. Furthermore, if the mean input is suprathresholded and the input fluctuations are weak, the ISI distribution is dominated by the periodicity of firing and is consequently narrow, approximating a Gaussian distribution.

Sgro et al. [33] published a model of single-cell and population dynamics; this model, supported by in vivo measurements, is able to describe the multiscale nature of the dynamics of molecular networks.

Noise influences biology at every level [32], from fundamental molecular and sub-cellular processes to the dynamics of neurons, tissues, organs, organisms, and populations. Its functional roles in biological processes can differ significantly.

Gupta et al. [34] published in 2020 a review paper focused on single-neuron models and related experiments, having the aim of understanding neuronal behaviour. The significance of single-neuron mapping and electrophysiological recording was highlighted, along with single-neuron isolation, manipulation, and therapeutic advancements using advanced micro/nanofluidic devices.

The Hindmarsh–Rose neuron model was analysed in 2020 by Ryashko and Slepukhina [35]; they analysed the transition from amplitude-modulated spiking to bursting induced by noise, using InterSpike Intervals statistics; they observed an increment of InterSpike Intervals due to the onset of noise-induced spiking–bursting transition.

The nonlinear dynamics of a FitzHugh–Nagumo model subjected to periodic excitation perturbed by noise were studied in Ref. [36]. In the unperturbed case, stable periodic orbits and bifurcation cascades follow Diophantine equations.

A Generalized FitzHugh–Nagumo system was analysed by Nkounga et al. [37] in 2023. The model considered an extension of the FHN neuron equation having multiple stable states, they showed that the noise can cause the switch of neural dynamics between different states: silence, subthreshold, and spiking.

The two-dimensional Rulkov model of neurons is based on the concept of maps, which is characterized by two chaotic regimes; one of them gives rise to neuronal bursting. In 2023, Lopez et al. [38] proposed a method for controlling the Rulkov model to allow a smooth transit from the chaotic regimes and increase the duration of bursting.

Wu et al. [39] considered a FitzHugh-Nagumo (FHN) neural network under electromagnetic induction. They provided a tool for interpreting information propagation through low-amplitude signals in a neural system.

Ref. [40] reported a numerical and experimental study of a memristor-based Hindmarsh–Rose neuron model, which is a multi-

Table 2
Mode shapes at room temperature, 28 °C.

Mode number	Mode type (m,n) m = longitudinal half-waves n = nodal diameters	Mode shape
1	First bending	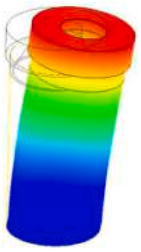
2	Torsional bending	
3	Torsional mode	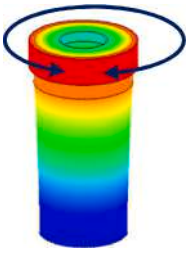
4	(1,0) first axisymmetric	
5	(1,1) second beam mode	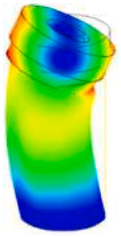
8	(1,5)	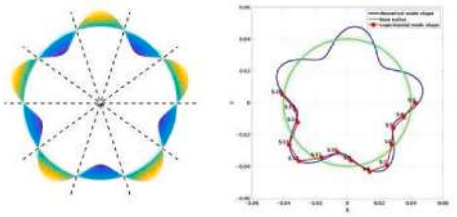

(*continued on next page*)

Table 2 (*continued*)

Mode number	Mode type (m,n) m = longitudinal half-waves n = nodal diameters	Mode shape
9	(1,6)	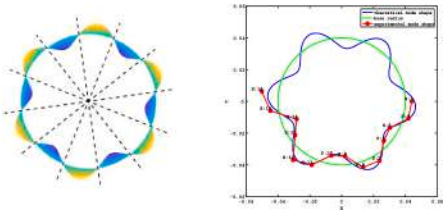
11	(1,4)	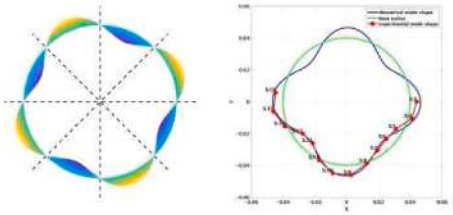
13	(1,7)	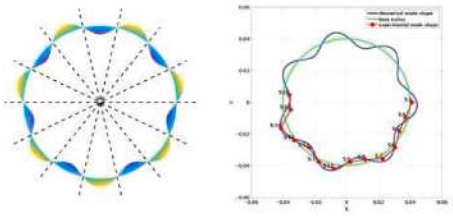
14	(1,3)	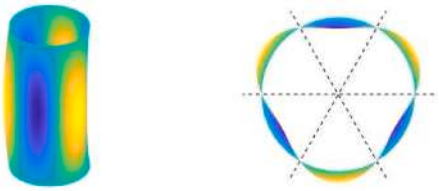
15	(2,6)	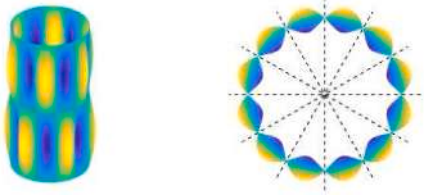
16	(2,7)	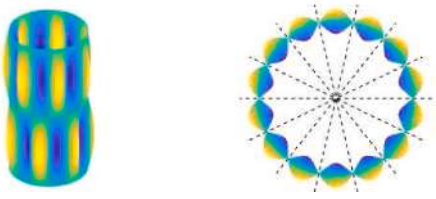

stability system; they detected the emergence of SuperExtreme Spiking (SES) oscillations. The same model was analysed in [41], this study examined the emergence of EE—rare, sudden, and high-intensity spikes triggered by noise within the system.

A review published in 2024 [42] analysed the last decades of research on FitzHugh-Nagumo model, they reported 323 papers focused on such an equation developed in 1960 for interpreting and simulating neural activity; they pointed out that such an equation was used for simulating heart physiology, cellular dynamics, population dynamics, electronic circuits, and other phenomena of natural science like Geology and Oceanography.

Hariharan et al. [43] clarified in 2025 that EEs induced by Ornstein–Uhlenbeck noise in a Fitzhugh–Nagumo oscillator system appear like a sequence of small and large-amplitude of oscillations characterized by an absence of periodicity; depending on noise level, the quiescence, i.e. the absence of bursts, tends to decrease. These phenomena are correlated with complex neuronal behaviours and are characterized by noise-driven stochastic bursting oscillations.

The analysis of the literature gives a clear view of the intense research carried out in the last decades on the complex phenomena

Table 3
First axisymmetric mode frequency and damping ratio vs. temperature.

First axisymmetric mode			Reference temperature 28 °C	
Temperature °C	Frequency Hz	Damping ratio %	Frequency variation %	Damping ratio variation %%
0	266,82	1,56	4,0 %	102,6 %
10	263,29	1,25	2,6 %	62,3 %
20	259,94	0,92	1,3 %	19,5 %
28	256,54	0,77	0,0 %	0,0 %
40	253,84	0,57	−1,1 %	−26,0 %
50	250,85	0,41	−2,2 %	−46,8 %

arising when a nonlinear system is subjected to direct or indirect noise excitation. On the other hand, the deep analysis of the literature also shows that phenomena like spikes, bursts, or extreme events are almost unexplored in the field of Solid Mechanics and, more generally, in mechanical systems, both in the macro and nanoscale. Even though structures like shells can exhibit extremely complex dynamics at macro [44,45] and nanoscale [46], showing chaotic response and an evident sensitivity to environmental conditions [47,48] or to interactions with fluids [49], unexpected phenomena arising from high energy random forcing are almost absent in the scientific literature except for Ref. [50], where a synchronization phenomenon was observed.

In the present work, we report a wide experimental analysis of a polymeric shell subjected to a purely random excitation, characterized by a limited frequency band (almost monochromatic noise), which shows evidence that Extreme Events (EE) can take place also in structural systems. The system under investigation is a circular cylindrical shell, excited seismically from the base along its longitudinal axis, such excitation gives direct forcing to axisymmetric modes and autoparametric excitation to the shell-like modes. Under extreme conditions, i.e., high forcing energy levels, the response to the random excitation exhibits unexpected spikes, which are irregular both in amplitude and temporal distribution. Such spikes present strong similarity with the phenomena observed in neuronal models, electronic circuits, laser waves, and rough waves; therefore, models based on van der Pol, Fitz-Hugh–Nagumo, Morris-Lecar, and Langevin are extremely important for interpreting the experimental evidence. The analysis of EE detected during the experiments revealed an oscillatory nature of spikes, with a spectral content coincident with the natural frequencies of the system, and a decay that appears similar to a transient response of the free oscillations of the structure. For such reason, we call the EE “Ghost Hammering”; indeed, it seems that an invisible impact excites the shell and generates the transient response.

In the paper, the experimental setup and the main characteristics of the system under investigation are described. A section is dedicated to the standard linear modal analysis that is fundamental for interpreting the subsequent section focused on the Stochastic Resonance and the main features of the Extreme Events.

2. Description of the problem and the experiment

The goal of this work is a deep investigation into the dynamics of circular cylindrical shells subjected to random excitation. In particular, to understand the effects of base excitation in circular shells, similar to actual situations taking place in space launchers or civil structures under earthquake, an experimental setup is developed to exert axial excitation having a stochastic nature.

Fig. 1a shows the experimental setup; a circular cylindrical shell is clamped at the base on a shaker, which imposes a vertical motion; the top of the shell is closed with a rigid disk, where three tri-axial accelerometers are mounted to measure the vertical, tangential, and radial acceleration. In Fig. 1a, the Laser measurement point is visible (red spot); here we measure the radial vibration of the shell without perturbing the system. The shell material is PET (polyethylene terephthalate), selected for its good flexibility, resilience under prolonged high-intensity vibration testing, and sensitivity to thermal conditions. The specimen consists of a cylindrical shell made of PET, characterized by a density (ρ_S) of 1366 kg/m^3 and a Young's modulus (E) of 3.2×10^9 Pa. The shell has a length (L) of 0.135 m, an external radius (R_e) of 0.040 m, and a wall thickness (h) of 0.38×10^{-3} m. A steel disk is mounted on top of the shell, with a mass (m_D) of 1.34 kg. The dimensions of the shell and upper disk are illustrated in Fig. 1b. The specimen is located inside a climate chamber to control the temperature during the tests.

The vertical motion imposed by the shaker to the base of the shell induces a rigid body motion and consequently, the inertial forces generated by the heavy top disk exert on the shell an axial action inducing membrane stresses and vibration; see Fig. 2, where the simplified scheme considers only the effect of the base motion. Clearly, in a real situation, when resonances are excited, the shell deformation can add a further contribution in terms of disk motion: three translations, two tilts, and a torsion around the cylinder axis. Note that, due to the special boundary conditions of the system, see Ref. [51], only the first axisymmetric mode, the beam-like modes, and the torsional modes involve the motion of the top disk; therefore, due to the vertical excitation, only the first axisymmetric mode is directly excited by a vertical seismic motion.

The schematic of the test setup is shown in Fig. 3, the main elements are: i) the specimen consisting of the polymeric shell; ii) the inertial element; iii) the shaker Dongling ET-40-370 (40 kN peak force, 100 g maximum acceleration, 500 kg max static payload, 1–2800 Hz frequency band); iv) the Laser Doppler vibrometer Polytec OFV-505 (25 m/s max velocity, 0.1 pm displacement resolution, 24 MHz frequency bandwidth); v) three integrated-electronics piezo-electric (IEPE) triaxial accelerometers (each having a mass of 5 g) mounted on the top mass and angularly spaced of 120° on the top disk (see also Fig. 1); vi) an IEPE monoaxial accelerometer glued on the Vibration Table Adapter (VTA) for measuring the drive excitation, which acts on the shell base; vii) the control/acquisition system, Siemens LMS Scadas with LMS Testlab

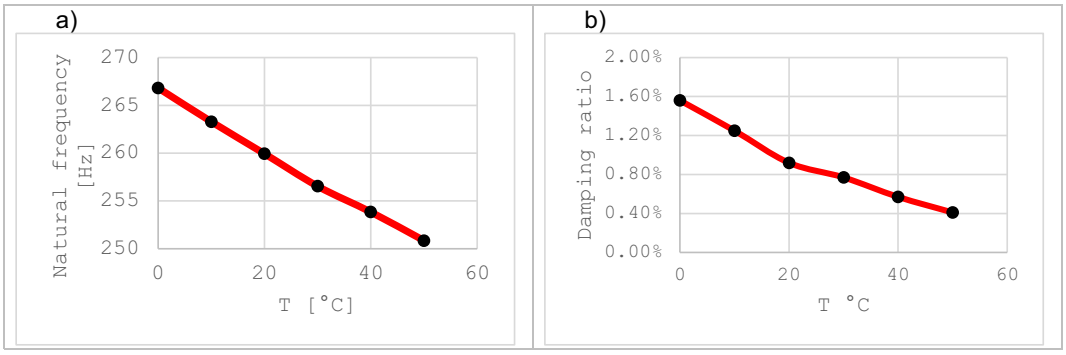

Fig. 6. First axisymmetric mode, modal properties vs. the temperature T °C.

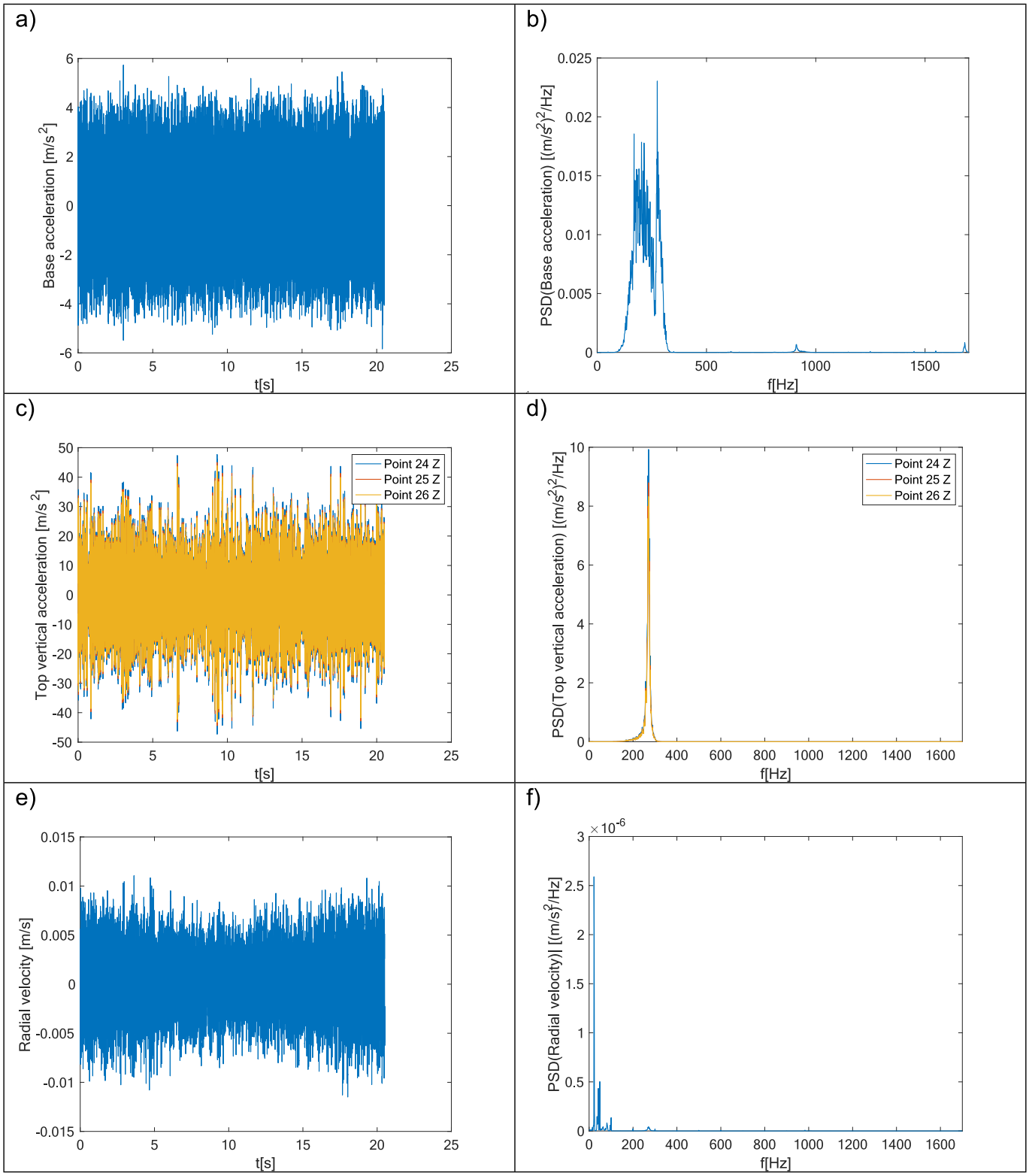

Fig. 7. Random test, low energy (0.01 V drive) T = 0 °C.

software; viii) a PCB micro hammer (model 086D80), with a vinyl tip, to carry out standard modal tests and parameter identification.

The setup allows controlling the vibration imposed on the specimen both in terms of overall amplitude and spectrum. The climate chamber associated with the shaker controls the temperature and humidity. The Laser Doppler measures the lateral vibration of the shell, which is the main interest of this work. The three tri-axial accelerometers located on the inertial top mass give: the magnitude of the average stresses induced to the shell by the inertial forces; the tilt of the top mass by checking differences between the three vertical accelerations; radial and tangential mass vibrations, which should be absent due to the symmetry of the system.

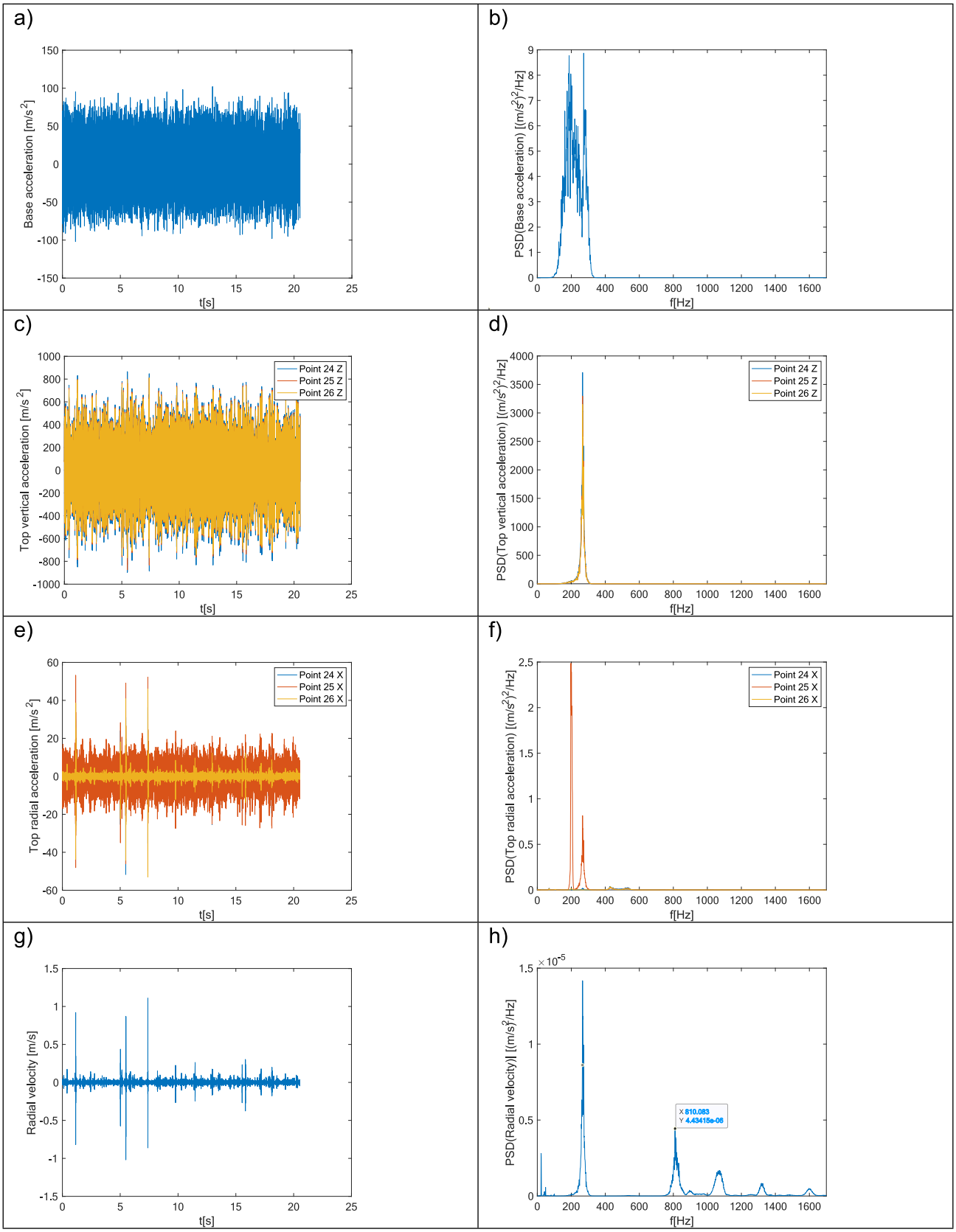

Fig. 8. Random test, high energy (0.225 V drive) T = 0 °C.

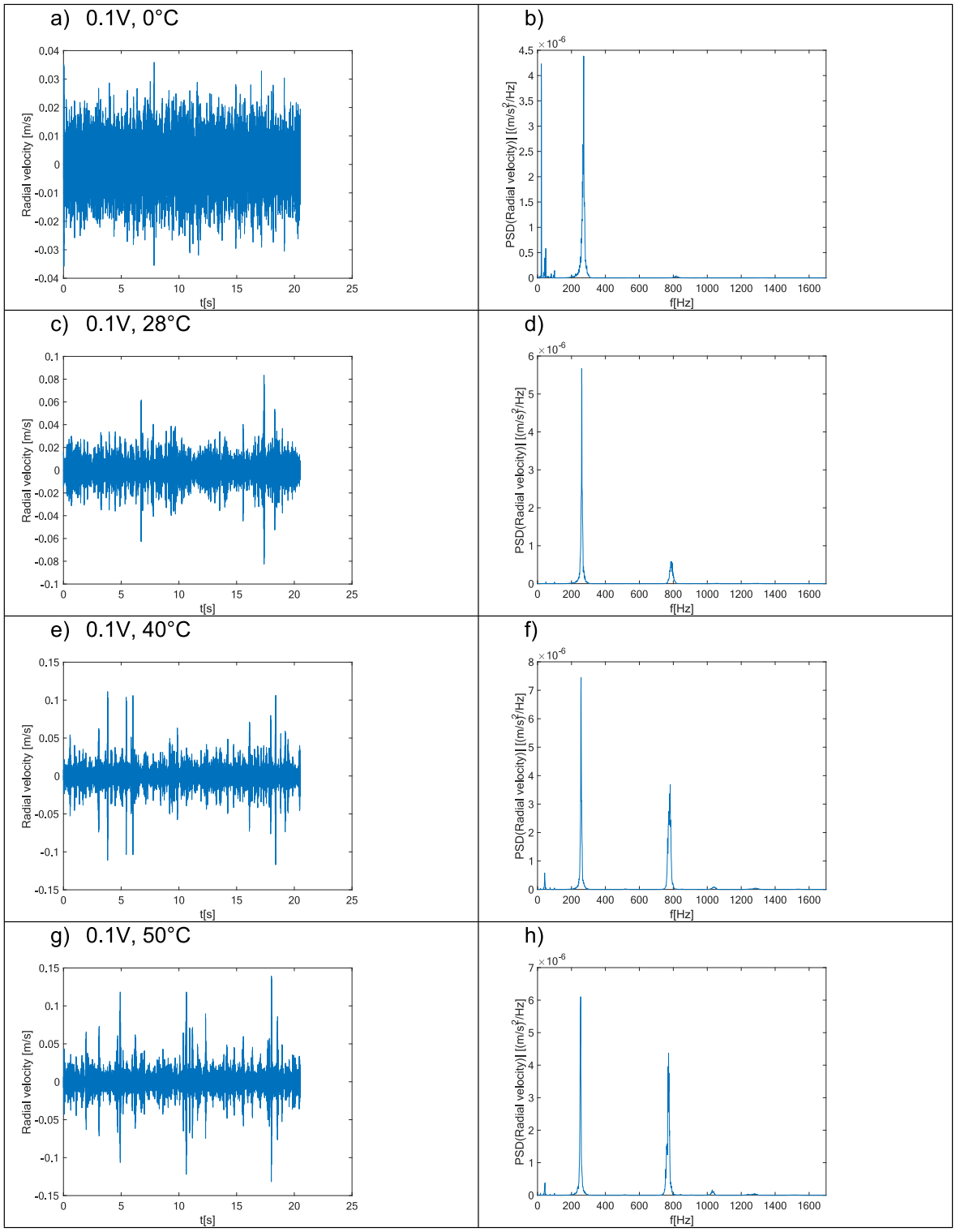

Fig. 9. Random test, high energy (0.1Vrms drive). a, b) T = 0 °C, c, d) T = 28 °C, e, f) T = 40 °C, g, h) T = 50°.

2.1. Static instability and parametric resonances

When structures like shells, panels, plates, or beams are subjected to high in-plane stresses, they can likely become unstable and undergo buckling. Curved shells are particularly sensitive to static instabilities, the pre and post-buckling behaviours can be incredibly complex, see the monumental work of Yamaki [52] or the review paper of Bushnell [53], who commented: "To the layman buckling is a mysterious, perhaps even awe-inspiring, phenomenon that transforms objects originally imbued with symmetrical beauty into junk". The origin of such complexity in shells, even in Statics, is due to the curvature, which induces the concurrent presence of quadratic and cubic nonlinearities; therefore, shells typically undergo strongly subcritical pitchfork bifurcation. An example is given in Fig. 4, reproduced qualitatively from Ref. [54], where the lateral deformation of an axially compressed circular cylindrical shell is represented vs. a normalized compressive axial load; the picture shows

Table 4
Frequencies and damping ratios vs. the temperature. Data extrapolated from mode 4.

Mode number	0 °C		10 °C		20 °C		28 °C		40 °C		50 °C	
	Natural frequency [Hz]	Damping %	Natural frequency [Hz]	Damping %	Natural frequency [Hz]	Damping %	Natural frequency [Hz]	Damping %	Natural frequency [Hz]	Damping %	Natural frequency [Hz]	Damping %
1	71,01	3,25	70,07	2,60	69,18	1,92	68,27	1,60	67,55	1,19	66,76	0,85
2	71,68	1,41	70,73	1,13	69,83	0,83	68,92	0,69	68,19	0,51	67,39	0,37
3	201,13	2,07	198,47	1,66	195,94	1,22	193,38	1,02	191,34	0,76	189,09	0,54
4	**270,37**	**1,34**	**266,80**	**1,08**	**263,40**	**0,79**	**259,96**	**0,66**	**257,22**	**0,49**	**254,19**	**0,35**
5	430,40	1,89	424,71	1,51	419,30	1,11	413,82	0,93	409,46	0,69	404,64	0,50
6	433,38	2,11	427,65	1,69	422,21	1,24	416,69	1,04	412,30	0,77	407,44	0,55
7	826,79	1,94	815,86	1,55	805,48	1,14	794,94	0,96	786,57	0,71	777,31	0,51
8	847,10	1,95	835,89	1,57	825,26	1,15	814,46	0,96	805,89	0,71	796,40	0,51
9	891,09	3,54	879,30	2,84	868,11	2,09	856,76	1,75	847,74	1,29	837,76	0,93
10	969,78	2,18	956,95	1,74	944,77	1,28	932,41	1,07	922,60	0,80	911,73	0,57
11	977,86	2,10	964,93	1,69	952,65	1,24	940,19	1,04	930,29	0,77	919,33	0,55
12	1092,48	2,11	1078,03	1,69	1064,31	1,24	1050,39	1,04	1039,33	0,77	1027,09	0,55
13	1106,53	2,15	1091,89	1,72	1078,00	1,27	1063,90	1,06	1052,70	0,79	1040,30	0,57
14	1326,48	2,34	1308,93	1,87	1292,27	1,38	1275,37	1,15	1261,95	0,85	1247,08	0,61
15	1453,65	2,47	1434,41	1,98	1416,16	1,45	1397,64	1,22	1382,93	0,90	1366,64	0,65
16	1482,41	2,22	1462,80	1,78	1444,19	1,31	1425,30	1,10	1410,30	0,81	1393,69	0,58
17	1503,33	2,37	1483,44	1,90	1464,57	1,40	1445,41	1,17	1430,20	0,87	1413,35	0,62
18	1591,48	2,33	1570,42	1,87	1550,44	1,37	1530,16	1,15	1514,06	0,85	1496,22	0,61
19	1645,12	2,34	1623,36	1,88	1602,70	1,38	1581,74	1,16	1565,09	0,86	1546,66	0,62

the cases of perfect and imperfect shells. In Fig. 4, the classical buckling load is considered for normalization, $P_{cl} = 2\pi \frac{Eh^2}{\sqrt{3(1-\nu^2)}}$, such a parameter is commonly used by engineers, even though it should be used with extreme care in the case of shells. To understand the complex dynamic phenomena described in the next section, it is useful to describe the buckling paths in detail.

2.1.1. Perfect shells

When the shell is compressed, initially undergoes an axisymmetric deformation due to the Poisson effect (see the blue line in Fig. 4); the lateral deformation is almost linearly dependent from the load up to the critical load, i.e. the bifurcation point, which is located at about 95 % of P_{cl}, because the simple formula of P_{cl} does not consider the pre-buckling bending deformation. Beyond the critical load, the "trivial" equilibrium loses stability; from the bifurcation point, a strongly subcritical branch bifurcates, which is unstable up to the saddle-node bifurcation, which is much lower than the critical load, for example, 50 % P_{cl} in Fig. 4, but can drop up to 25–30 % for bigger imperfections.

2.1.2. Imperfect shells

It is well known that the pitchfork bifurcation is structurally unstable, i.e., it is destroyed by perturbations. In the case of shells, the perturbation in terms of geometric imperfection transforms the pitchfork bifurcation into a saddle-node bifurcation and strongly reduces the critical load. Even when imperfections are present, the behaviour remains strongly subcritical. Such kind of post-critical path means that, even if the compressive load is much smaller than the critical one, the system can jump to high deformations due to the coexistence of multiple equilibria.

Soedel [55] suggested a simple formula for estimating the dependency of natural frequencies of a simply supported shell from the compressive load:

$$\omega_{m,n}^2(P) = \omega_{m,n,0}^2 - \frac{P}{2\pi R \rho_S h}\left(\frac{m\pi}{L}\right)^2 \tag{1}$$

where $\omega_{m,n}$ is the circular frequency (rad/s) of the mode having n nodal diameters and m longitudinal half waves, $\omega_{m,n,0} = \frac{E}{(R^2\rho_S)}\left\{\frac{\left(\frac{m\pi R}{L}\right)^4}{\left(\left(\frac{m\pi R}{L}\right)^2+n^2\right)^2} + \frac{\left(\frac{h}{R}\right)^2}{12(1-\nu^2)}\left[\left(\frac{m\pi R}{L}\right)^2+n^2\right]^2\right\}$ is the natural frequency without axial load, E is the Young modulus, ρ_S is the mass density, L, R and h are the shell length, radius, and thickness, respectively.

When a circular cylindrical shell is subjected to a dynamic axial load $P + P_D\cos(\omega t)$, where the static part P is intended compressive, it can undergo a Mathieu-like dynamic instability. The imperfections do not create a dramatic effect when the static load P is absent, see Fig. 5, which reports qualitatively the findings of Ref. [54].

This introduction to the problem is needed for interpreting the experimental evidence of unusual phenomena that will be shown in the next section because there is a strict correlation between the Extreme Events recorded under high-energy Random noise tests and the natural tendency of shells to lose stability.

3. Modal analysis

For understanding any complex dynamic scenario arising from nonlinearities and resonances, the knowledge of the spectral properties of the system is indispensable. In this work, a series of tests have been carried out to identify natural frequencies, damping ratios, and mode shapes of the modes that are supposed to be involved in the nonlinear dynamic phenomena appearing at high energy.

Two series of tests are carried out:

1. Impact hammer tests. The shell is excited by a micro hammer that can measure the low-level force exerted, the vibration is measured in four points: a point on the shell (Laser), and three points on the top (accelerometers). The excitation is repeated at several points along one generatrix of the cylinder. All modes in the band of excitation are identified with this procedure. The tests are carried out a room temperature.
2. Base excitation. The shell is excited from the base using a low-level broadband signal. The response is measured on the shell (one point) and the top (three points). This excitation, at a low level, can provide energy to the first axisymmetric mode only, therefore, only this mode is identified. Tests are repeated in a climate chamber so

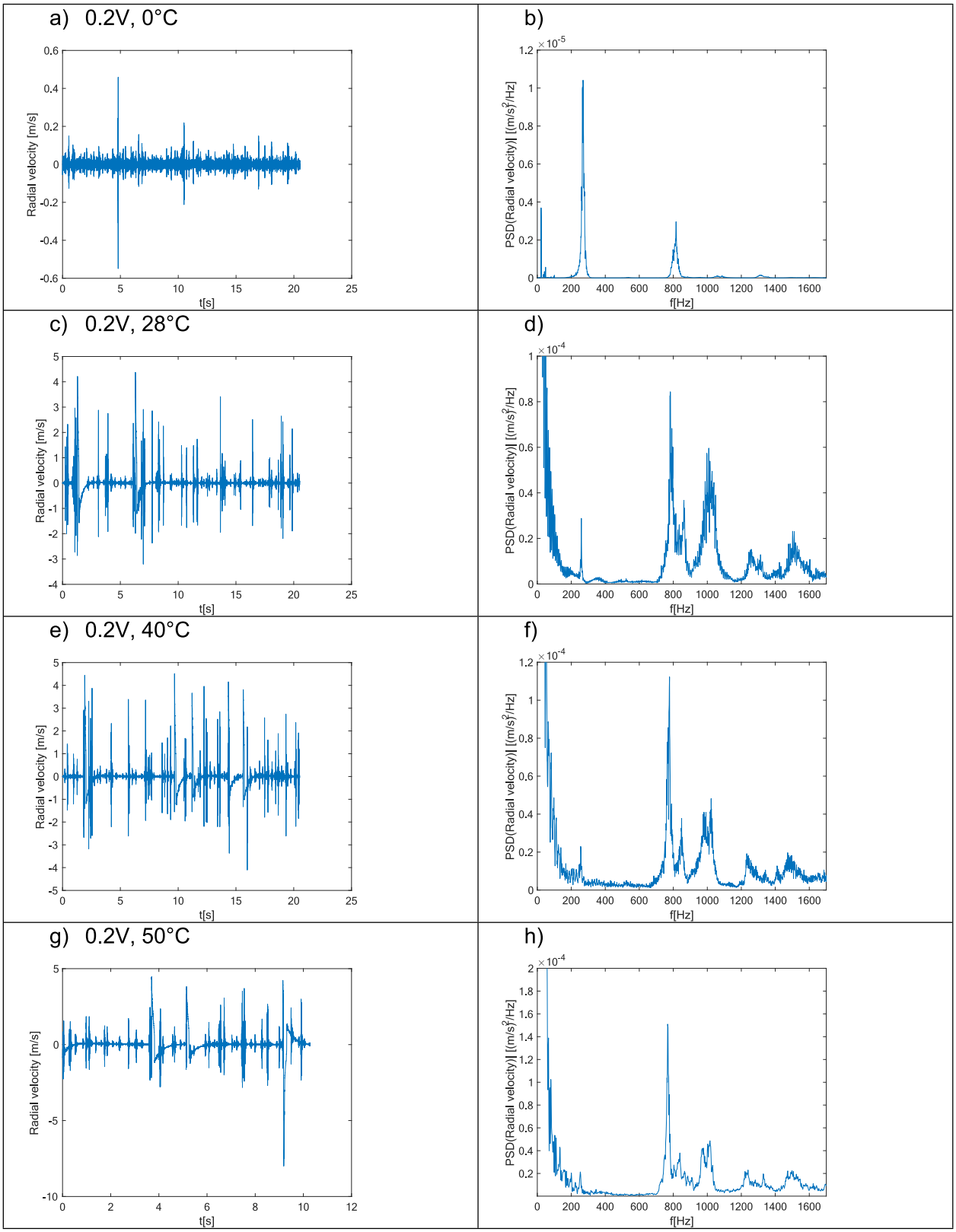

Fig. 10. Random test, high energy (0.2Vrms drive). a, b) T = 0 °C, c, d) T = 28 °C, e, f) T = 40 °C, g, h) T = 50°.

that the axisymmetric mode is identified in a wide range of temperatures.

Using the information obtained from the axisymmetric mode at different temperatures, we can extrapolate the natural frequencies and damping ratios of all modes as the thermal conditions vary.

In Tables 1 and 2, the results of the full modal analysis at room temperature are presented; the tests are carried out using procedure 1, i.e., impact hammer, providing a comprehensive overview of the system's dynamic characteristics. Natural frequencies, damping ratios, and

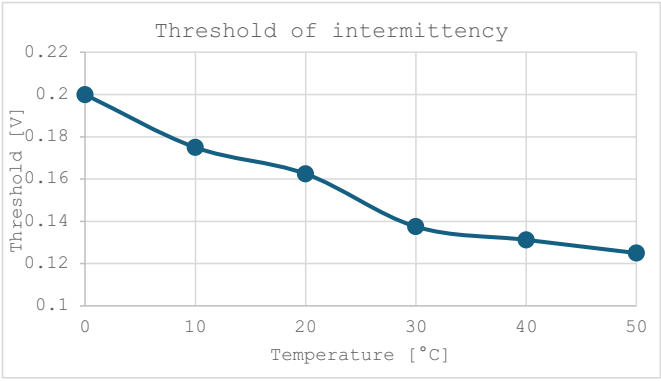

Fig. 11. Random test, 110–320 Hz excitation band. Threshold of the Ghost Hammering phenomenon.

modal shapes are given. The first five modes involve the motion of the top mass; however, only mode 4, the first axisymmetric mode, displays a vertical top mass motion, and the other beam-like modes show a lateral or rotational displacement. This implies that, from a vertical base excitation, only the axisymmetric mode (1,0) is directly excited. Higher frequency modes are essentially shell modes, for such modes the top rigid disk acts like a clamping; therefore, for these modes, the boundary conditions can be considered clamped at both ends, see Ref. [51] for details. Even shell modes are not directly excited by a base vertical motion.

Regarding the mode shapes presented in Table 2 modes from 1 to 5 and modes from 14 to 16 are illustrated based on the results of the experimental modal analysis. For modes 8, 9, 11, and 13, the experimental modal shapes have been compared with the theoretical modal shape, and both are shown graphically.

In order to characterize the spectral properties of the system vs. the temperature, test procedure 2 is carried out, from 0 °C to 50 °C; results are listed in Table 3, the increment of temperature causes a reduction of the natural frequencies and the damping ratios, however, the max variation of the frequency is 4 %, conversely, the variation of damping ratio reached about 100 %; Fig. 6a and b shows that the decrement of natural frequencies and the damping ratio is almost linear. The temperature dependence of the damping strongly influences the response of the system in resonance and the onset of nonlinear complex phenomena.

Using data from Tables 1 and 3, the natural frequencies and damping ratios of all modes at different temperatures are rescaled with the same % variations of the reference temperature of 28 °C.

4. High energy random tests and data analysis

The first test is carried out at 0 °C, exciting the system with a random base motion limited at the band frequency (110- 320 Hz), this band will excite the first axisymmetric mode (270 Hz, mode 4). The input is given with an RMS (Root Mean Square) of 0.01Vrms of the signal sent to the shaker amplifier, this value is correlated to the real base vibration through the transfer function of the shaker-amplifier, see Ref. [56] for details, here the value of the input signal is useful for understanding the differences between different tests in terms of vibration energy, the real base amplitude can be read by the signal recorded from the accelerometer located on the VTA, i.e. the base acceleration. In Fig. 7a and b, one can see the excitation time history and its spectrum, where most of the energy is concentrated on the theoretical band (110-320 Hz). The time history of the top disk, Fig. 7c, is similar to the excitation, i.e. stationary random process; its spectrum presents a well-defined maximum at 266 Hz (Fig. 7d), i.e., the resonance of mode 4, as expected for a linear system. Due to the high concentration of energy in the top disk vertical vibration, the signal represented can be classified as "monochromatic noise". It is worthwhile to note that the excitation of the shell is mainly due to the axial forces applied to the shell from the top disk, which are strictly proportional to the inertia forces generated by the mass motion. Note that in the spectrum of the top mass, higher contributions are completely absent, which means that the dynamics of the first axisymmetric mode are acting as a low-pass filter. The vibration of the shell, Fig. 7e and f, is coherent with the stationary random character of the excitation; this lateral vibration is due to the linear effect of the lateral deformation caused by the Poisson effect. For such a low level of vibration, the response of the system follows the typical behaviour of linear systems, with an overall amplification of about 10 due to the presence of a resonance in the excitation band.

Now we increase the input level from 0.01Vrms to 0.225Vrms, which means about 20 times more than the previous case. The temperature is set at 0 °C, like the previous case, therefore we are exciting again the first axisymmetric mode (270 Hz, mode 4). The vibration signals of the base vibration and the vertical vibration of the top mass are qualitatively similar to the low energy experiment (Fig. 8a–d) when the system responded linearly; therefore, if the system analysis were stopped here, nothing relevant would have to be observed. Conversely, the vibration of the top mass in the radial direction, as well as the vibration of the shell, reveals a completely different and surprising scenario, Fig. 8e–h. The radial vibration of the top disk presents a background noise character of order of $20\frac{m}{s^2}$, Fig. 8e (in the case of low energy the level was about $1\frac{m}{s^2}$, coherently with the difference in the input signal which is now 20 times bigger); moreover, the random signal is interrupted by spikes having an irregular time distribution, the spikes reach $50\frac{m}{s^2}$, i.e. the maximum radial vibration of the top mass is now 50 times bigger than the case at low energy (0.01Vrms v.s. 0.225Vrms). The analysis of the shell vibration presents similar characteristics of the radial top mass vibration, background noise with irregularly distributed spikes; note that the maximum level of vibration is now 100 times the one at low energy, even if the difference in the input signals is 20. Such spikes have an oscillating nature, like an invisible hammer that impacts the shell, for such reason, we call them the **Ghost Hammering phenomenon**. The spikes introduce frequency components corresponding to modes 4, 7, 12, 14, and 18; therefore, we can claim that an auto-parametric stochastic resonance can be the activation mechanism of these Extreme Events.

In Fig. 9, the effect of temperature is shown; tests are carried out with an input of 0.1Vrms, and four temperatures are considered: 0, 28, 40, and 50 °C. As shown in Table 4, the natural frequencies are not very sensitive to the temperature, conversely, the damping ratio shows a large decrement. We can see that at 0 °C, the shell vibration is dominated by random noise having a maximum amplitude lower than $0.04\frac{m}{s}$; in the spectrum, the main peak is located at 272 Hz (mode 4, resonant), at higher frequencies, the level is almost negligible. At 28 °C, the shell vibration still presents a normal random character, even though some small spikes seem to appear; the spectrum is still dominated by the resonance peak of mode 4, which is now at 260 Hz, and a small peak is now evident at 780 Hz, corresponding to the frequency of mode 7. By increasing the temperature up to 40 °C, the dynamics take another nature, the time history shows several spikes of amplitude larger than $0.1\frac{m}{s}$ and the frequency content is no longer dominated by the resonant axisymmetric mode 4, the peak at 256 Hz, but the harmonic energy also concentrates around the peak at 781 Hz, which again corresponds to mode 7. The highest temperature tested, 50 °C, shows strong evidence of spikes, and the two main peaks in the spectrum are 253 and 772 Hz.

For a higher energy level of excitation, 0.2Vrms drive, the scenario is clearer and perhaps surprising, Fig. 10. At 0 °C, strong spikes up to $0.4\frac{m}{s}$ takes place, and the spectrum shows peaks at 269 and 817 Hz, i.e., modes 4 and 7 that were also evident at 0.1Vrms drive. Increasing the temperature to 28 °C causes a strong increment of the frequency of spikes and their amplitude, which now reaches $4\frac{m}{s}$; in the spectrum, the frequency of mode 4 almost disappears and the energy is concentrated at 781, 862, 1010 Hz, i.e., modes 7, 9, 12. This means that now there is a

complete energy transfer from a band-limited random excitation to specific harmonics, the energy in the excitation band 110- 320 Hz seems completely lost in the response. For higher temperatures, 40 and 50 °C, the situation appears similar to the case at 28 °C, confirming that, once the threshold is exceeded, the ghost hammering phenomenon is stable and maintains its overall character.

Fig. 11 shows the threshold of Ghost Hammering appearance in terms of input drive voltage vs. the temperature. It seems that the threshold follows the decrement of the damping ratio, with an almost linear dependence on the temperature.

Now the temperature T = 40 °C is considered to check the change in the dynamics when the energy of excitation increases. Initially, an input

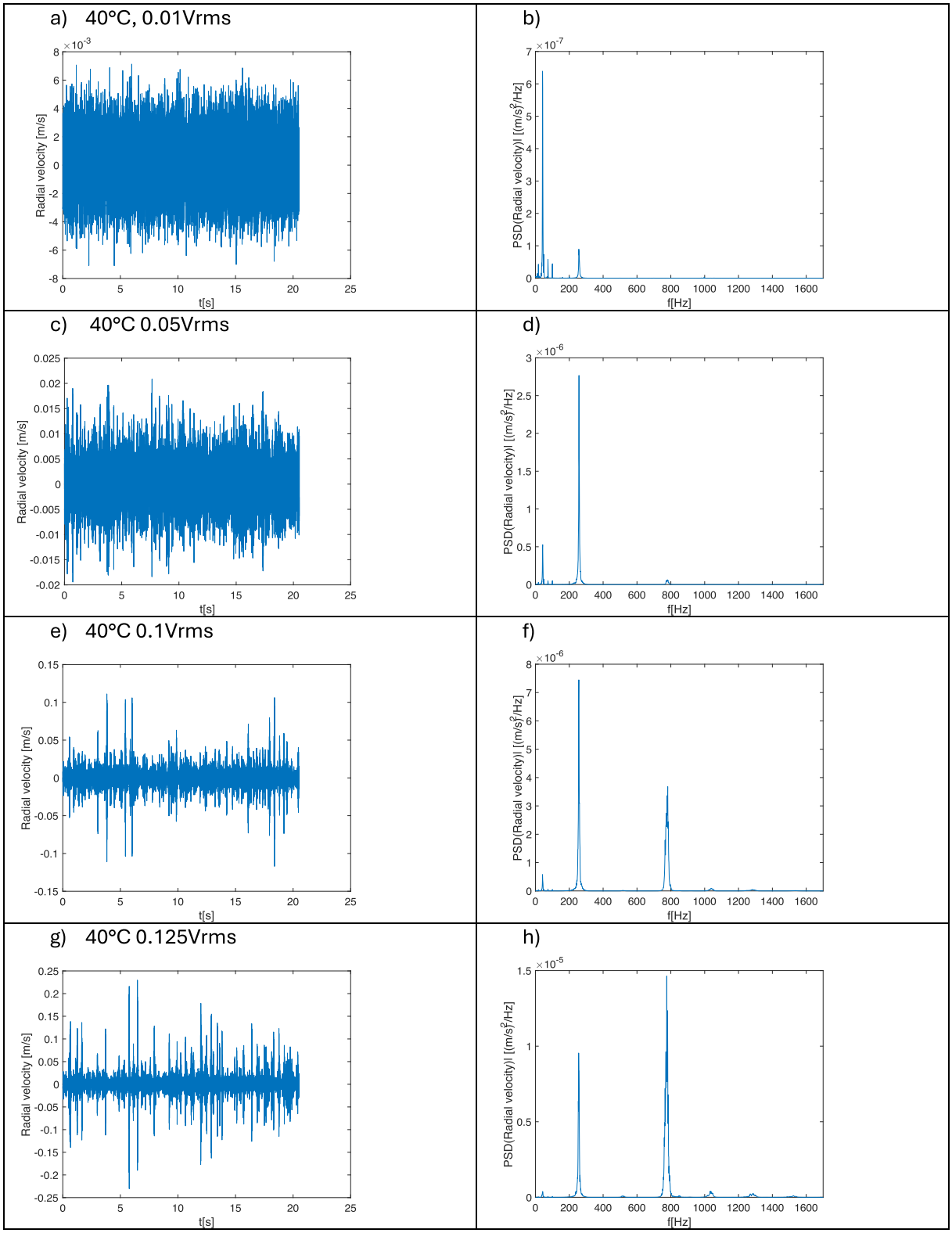

Fig. 12. Random test, T = 40 °C. a, b) 0.01Vrms; c, d) 0.05Vrms; e, f) 0.1Vrms; g), h) 0.125Vrms; i, j) 0.15Vrms; k, l) 0.2Vrms.

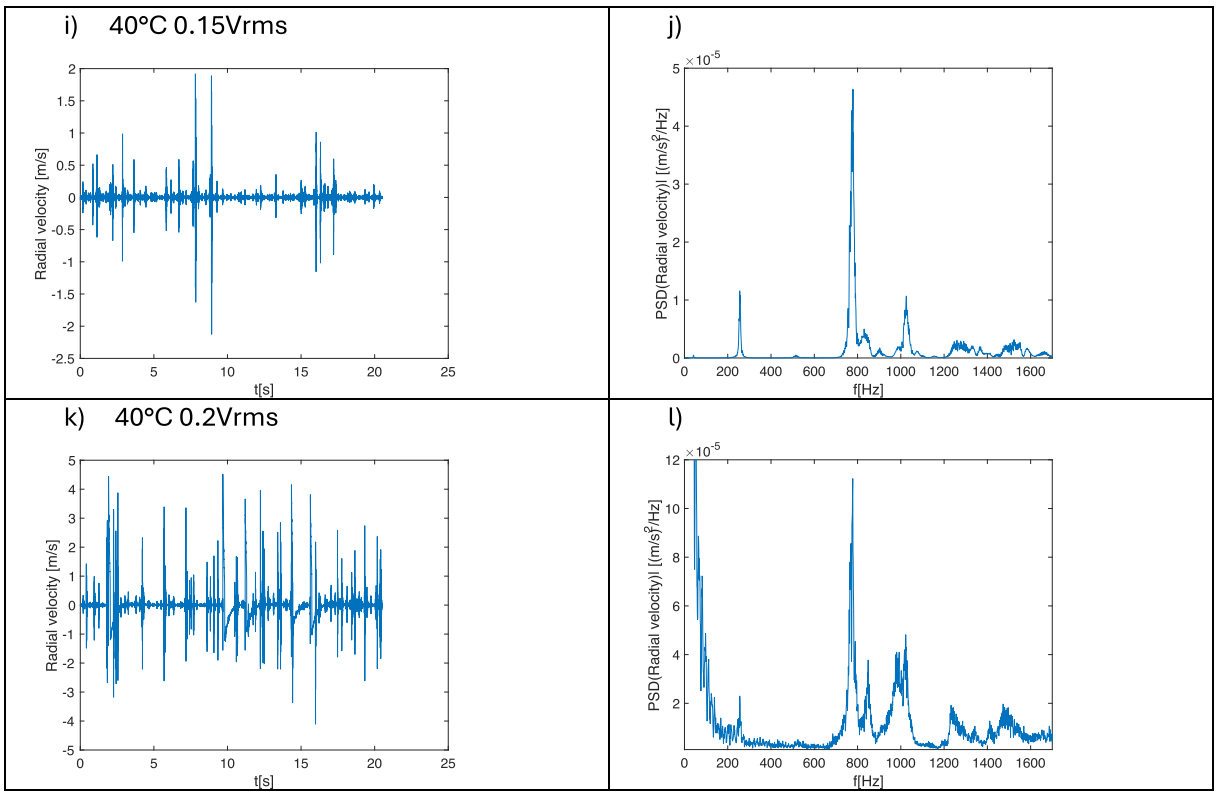

Fig. 12. (*continued*).

drive of 0.01Vrms is considered, the response of the shell is purely random, see Fig. 12a and b; a small peak at 256 Hz, corresponding to mode 4, is present in the spectrum, and the response is dominated by noise. For the input drive equal to 0.05Vrms, an almost pure random response is measured, a main peak at 256 Hz (mode 4) is present in the spectrum, a secondary peak at 781 Hz is also visible (mode 7), and other spectral content at higher frequencies is marginal. Increasing the input up to 0.1Vrms determines a qualitative change in the response; the time history shows the presence of small spikes, the spectrum clearly shows peaks at 256 Hz (mode 4), 781 Hz (mode 7), 1039 Hz (mode 12), and 1282 Hz (small activation of mode 14). When the drive reaches 0.125Vrms, spikes become more frequent in time and their amplitude slightly increases, the spectrum shows peaks at 255 Hz (mode 4), 513 Hz (twice the frequency of mode 4), 776 Hz (mode 7), 1032 Hz (mode 12), 1284 Hz (small activation of mode 14). Once the drive reaches 0.15Vrms, the presence of spikes in the time history is fully developed, their amplitude increases 10 times; now the spectrum is greatly changed, the peak at 255 Hz (mode 4) is less relevant, the harmonics at 513 Hz is marginal, mode 7 at 779 Hz dominates the spectrum, followed by a small peak at 830 Hz, and an evident peak at 1025 Hz (mode 12). The scenario for the maximum drive tested, 0.2Vrms, is more interesting; spikes increase in amplitude reaching the notable level of 4 m/s with a high frequency even irregularly distributed in time; the spectrum shows that the peak at 255 Hz (mode 4) is almost disappeared, the background spectral noise is dominant with evident peaks at 778 Hz (mode 7), 849 Hz (mode 9), 980 Hz (mode 11), 1022 Hz (mode 12), 1232 (small activation of mode 14), 1473 Hz (probably mode 17).

From this analysis, it is clear that the activation of the stochastic resonance caused not only the onset of irregularly spaced spikes but also that such spikes are driven by the energy that flows from the exciter, the base motion, to the axisymmetric mode (mode 4) that is directly excited. An auto-parametric stochastic resonance driven by mode 4 activates high-frequency shell modes. Indeed, when the excitation level increases, there is a change both in time response and spectrum; the latter shows that increasing the energy leads to the activation of frequencies coincident with the natural frequencies of the system. We can see that the noise is conveyed to some specific frequencies corresponding to the natural frequencies of the system. This is confirmed at different temperatures and excitation levels.

It is noted that the classical buckling load of the shell under investigation is $P_{cl} = 1782$ N, considering a knockdown factor of 0.3, see Fig. 4, when a compressive static axial load exceeds $P_{danger} = 30\%P_{cl} = 535$N, the shell can undergo to catastrophic buckling. The shell is in a vertical position, the top mass is 1.34kg, i.e. the static compressive load is negligible: 13.1N ($0.7\%P_{cl}$). In dynamic conditions the situation changes. At low energy, e.g. $T = 0^{\circ}$C drive 0.01Vrms, the maximum base acceleration is about $5\,\frac{\mathrm{m}}{\mathrm{s}^2}$ and the maximum top disc acceleration is about $40\,\frac{\mathrm{m}}{\mathrm{s}^2}$; the latter implies a maximum dynamic force of 54N (3 % P_{cl}). The situation changes completely at high energy, for example at $T = 0^{\circ}$C drive 0.225Vrms, the maximum base acceleration is about $100\,\frac{\mathrm{m}}{\mathrm{s}^2}$ and the maximum top disc acceleration is about $800\,\frac{\mathrm{m}}{\mathrm{s}^2}$; therefore, maximum dynamic force is 1072N (60 % P_{cl}), higher than the threshold defined by $P_{danger} = 30\%P_{cl} = 535$N.

Even though the system does not have multistable equilibria, because the static compressive load is negligible, it continually and randomly experiences an axial variable load, that, for a certain period, creates a coexistence of three stable equilibria. It seems that the temporal distribution of spikes is not correlated with the threshold excess; however, in the short time intervals when coexisting equilibria exist, the shell could experience Benzi's Stochastic Resonance [5].

Now, it is interesting to better understand the nature of the spikes and how the peaks in the spectrum, corresponding to the natural frequencies, are activated. For such reason, in the next subsection, a local analysis of the spikes in the time domain is carried out to better understand their real nature.

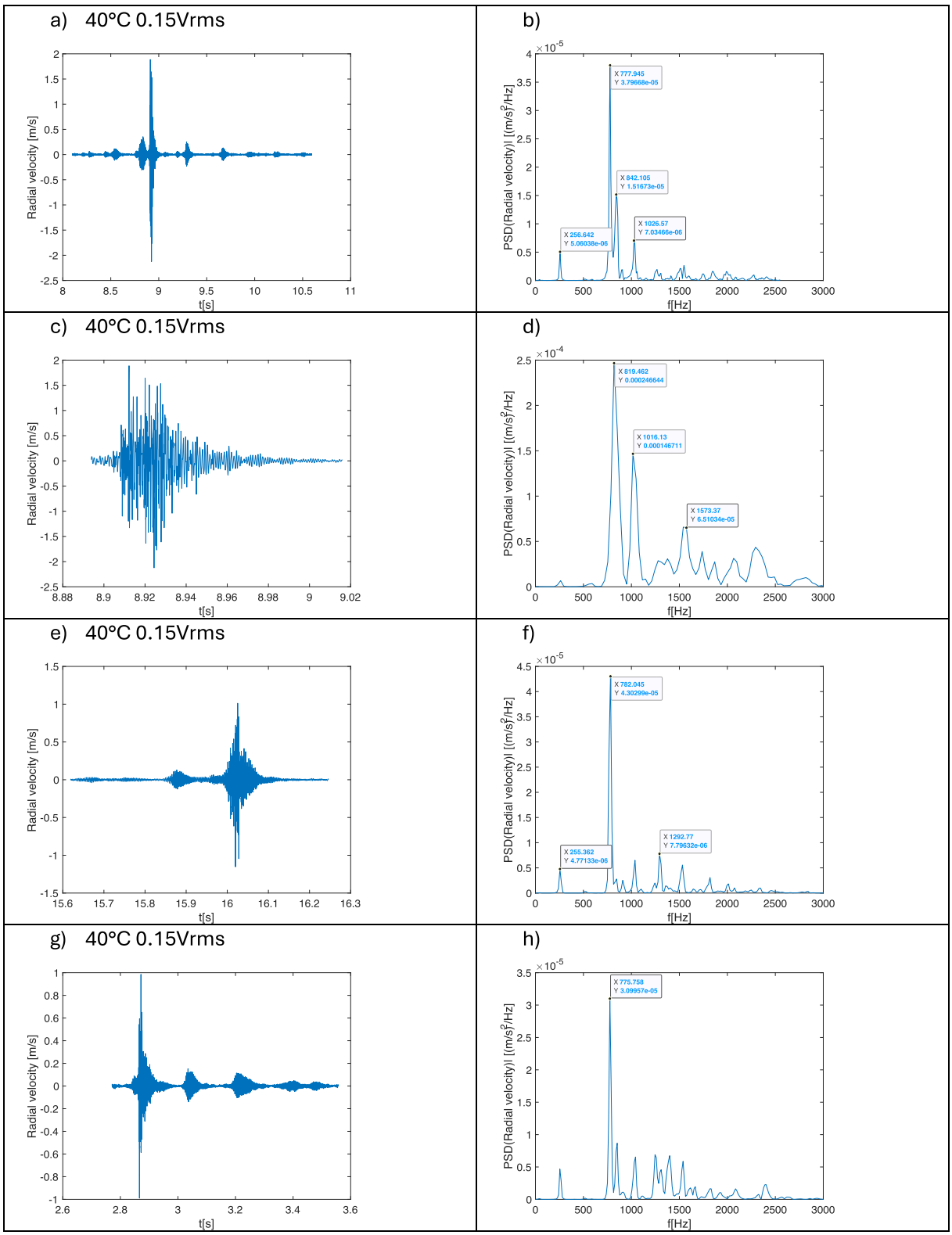

Fig. 13. Random test, T = 40 °C, drive 0.15Vrms, analysis of Extreme Events.

4.1. Analysis of Ghost Hammering

In this section, a deep analysis of the spikes observed at high levels of energy is carried out to clarify the nature of the Extreme Events.

Let us consider the case of Fig. 12i, where the excitation exceeded the threshold identified in Fig. 11 and the response presents strong spikes; the temperature is $T = 40^{\circ}$C, and the drive is 0.15Vrms. By zooming in the interval 8 – 11s, Fig. 13a, we observe that the EE is announced by small bursts and appears oscillatory. By carrying out a spectral analysis of the response in this time window, we can see that the spectral content corresponds to modes: 4 (low level), 7 (dominant), 9, and 12. The oscillatory nature is visible in the narrower zoom, Fig. 13c; the spectrum

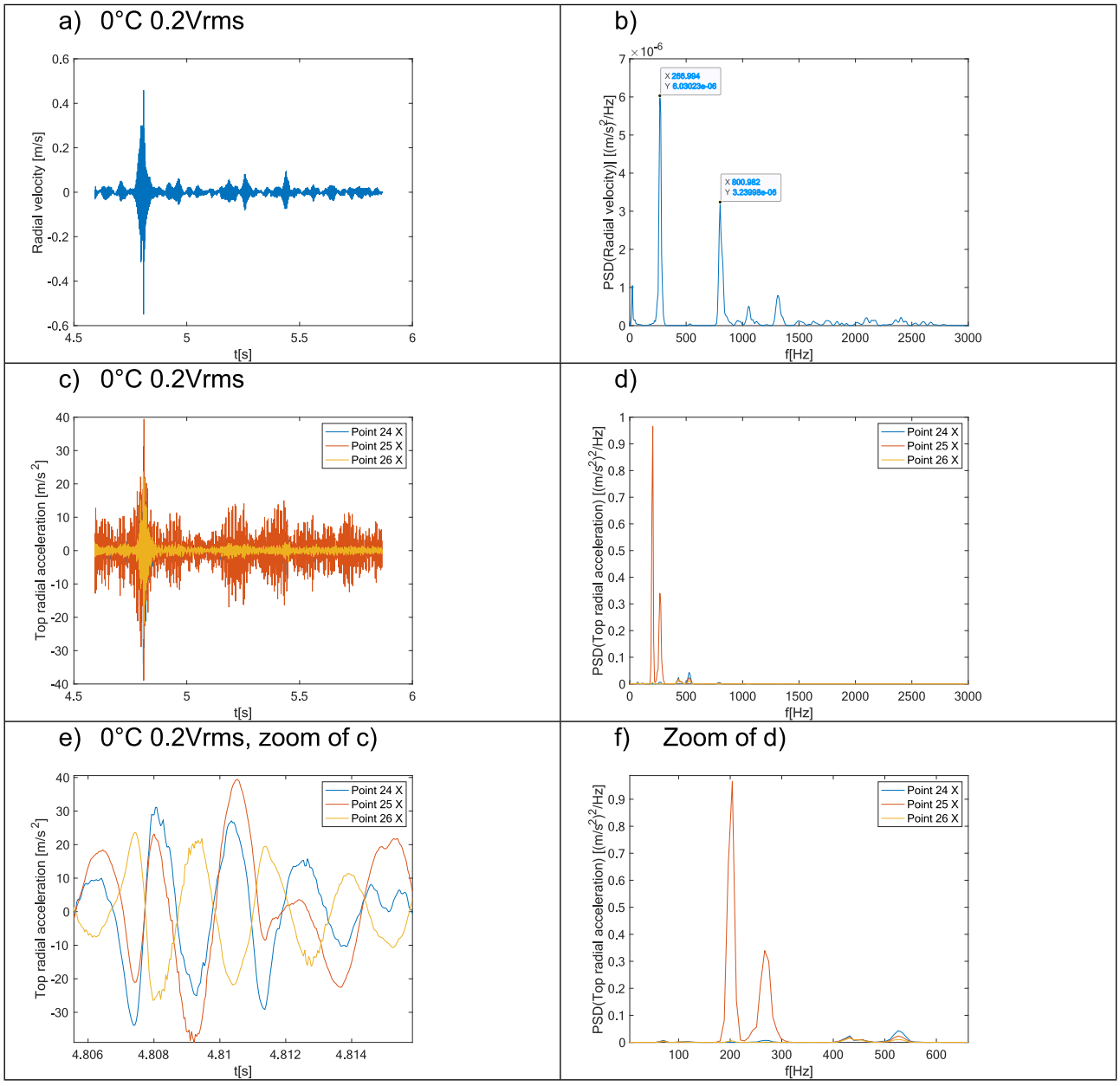

Fig. 14. Random test, T = 0 °C, drive 0.2Vrms, analysis of Extreme Events.

of such narrow zoom, Fig. 13d, confirms the aforementioned spectral content, even though using a window of 0.13s and four averages for the Power Spectral Density, we have a spectral resolution $\Delta f = 32.77$Hz, so in this case the two spikes at 778 Hz and 842 Hz are here practically merged.

Another EE of Fig. 12i is observed at about 16s, the zoom of the burst is shown in Fig. 13e; here the burst amplitude is lower than in the previous case, but the spectral content is similar, see Fig. 13f, with the dominance of mode 7. Similar behaviour is observed for the EE appearing at 2.85 s, see Fig. 13g and the spectrum of Fig. 13h.

To cross-check the nature of the spikes manifested at different temperatures, the case at 0 °C and 0.2Vrms drive is considered, see Fig. 10a; the spike at 4.5 s is analysed, the zoom is shown in Fig. 14a; even in this case the EE presents an oscillatory nature, but here the dominance is addressed to mode 4, see the spectrum of Fig. 14b, with a small contribution of mode 7. To complete the inspection, the signals recorded by accelerometers located on the top mass are analysed, for the same environmental conditions; the radial directions are considered as in the other directions, spikes are not detected. Fig. 14c shows the radial vibration of the top mass, the EE is detected and the intensity is relevant, the spectrum shows, however, the presence of mode 3, which was not detected by the laser measurement on the shell. Another interesting feature of the signals, which apparently are uncorrelated, is that precisely close to the paroxysm of the event, the signals are almost synchronized: accelerometers in locations 24 and 25, blue and red lines of Fig. 14e are in-phase, and the signal 26, yellow line, in counter phase. Note also that, only close to the paroxysm, all three accelerometers detect a high level of vibration; most of the time, point 25 gives the most relevant level of vibration.

Fig. 15 shows that the accelerometric signals during the spike are strictly correlated, conversely, such correlation is completely lost far from the spikes.

The analysis of the extreme events observed in this investigation reveals clearly that the spikes induced by a random noise are driven by nonlinear phenomena that start from the activation of a vibration mode, the axisymmetric mode 4, which is the only one that receives energy

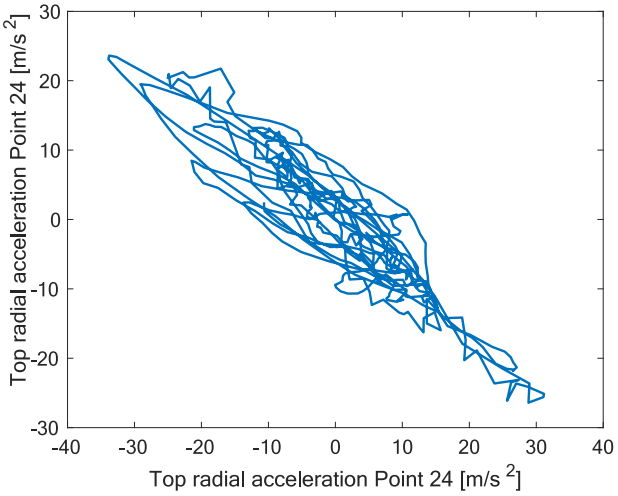

Fig. 15. Random test, T = 0 °C, drive 0.2Vrms, correlation between accelerometric signals. EE at $t = 4.81$ s.

from the base and activates a dynamic instability in higher frequency modes. The dynamic mechanism appears as a stochastic activation of resonances, which suddenly boosts some modes of vibration, similar to the typical activation experienced by structures when they receive an impact, for such reason, in the context of Structural Mechanics, we call the phenomenon **Ghost Hammering (GH)**.

The nature of Ghost Hammering presents strong similarities but also remarkable differences with respect to Stochastic Resonances analysed in most of the studies focused on neural impulses, electronic circuits, networks, or ocean waves [23–43], where the spikes have a non-oscillatory character and are driven to the overcoming of a known potential well. The model published by Brouwers [15] seems to give a theoretical model that could be used for understanding the experimental evidence of GH, he studied a Mathieu equation with stochastic forcing and the influence of noise for the onset of instabilities; however, he found four types of responses: one response fades away over time, another settles into random behaviour, and the last either keeps growing forever or suddenly drops to zero. Even in such a study, no oscillatory states are predicted.

The signals show that the EE (apparent spikes), observed during the experimental campaign, have an oscillatory: they are bursts of multi-harmonic oscillations with similar spectral content coincident with the natural frequencies of the system. Therefore, in this paper we have proven that a purely random excitation, can give rise to a dynamics having a deterministic content; the randomness of the phenomenon stays in the irregular temporal distribution of the bursts.

4.2. *Analysis of the signal's complexity: Spectral Entropy (SE)*

Here, the complexity of the phenomena described in the previous sections is analysed to gain a further understanding. The concept of Entropy of signals was introduced by Kolmogorov [57] to classify dynamical systems and determine the changes in signal complexity as well as address system randomness and regularity [58]. Here we use the Spectral Entropy algorithm of Matlab® [59–64], which evaluates the distribution of frequencies in the spectrum of the signal. This version of the concept of Entropy is particularly suitable for the phenomena under investigation, due to the oscillating character of the Extreme Events observed during the experiments. The normalized Spectral Entropy SE is briefly described below:

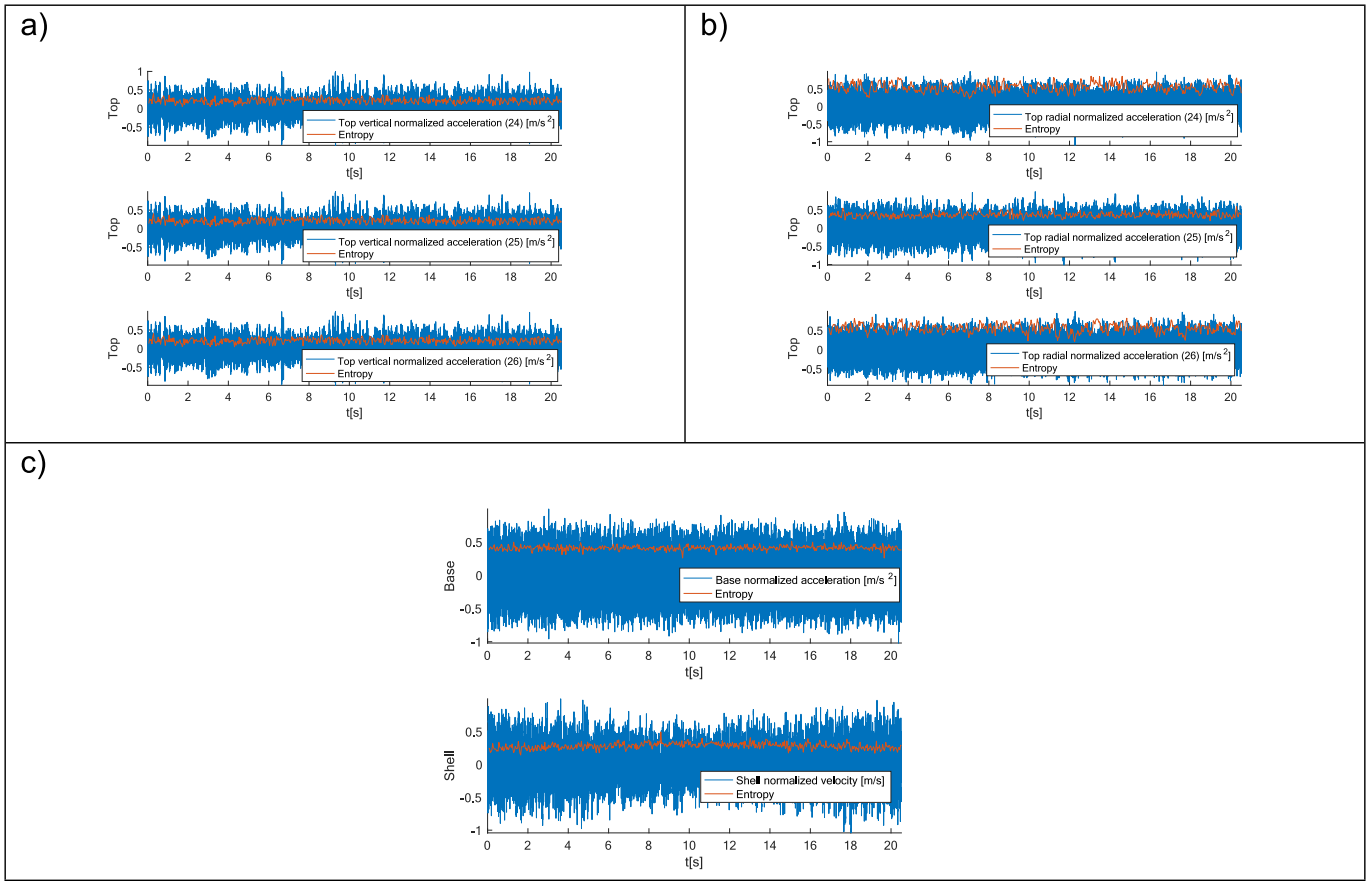

Fig. 16. Entropy of the random signals: drive 0.01Vrms temperature T = 0 °C.

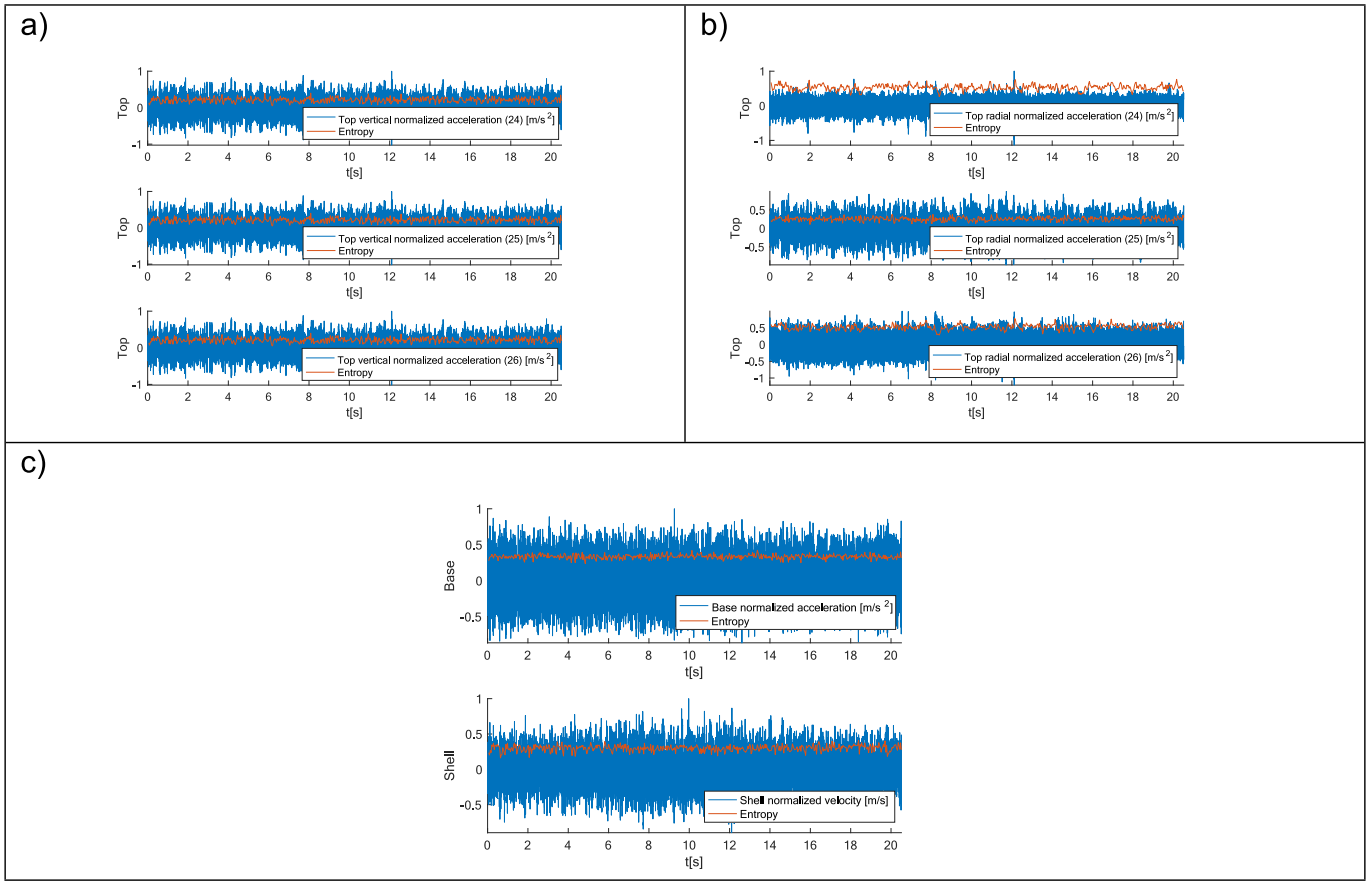

Fig. 17. Entropy of the random signals: Drive 0.05Vrms, temperature 0 °C.

$$SE = -\frac{\sum_{i=1}^{N} p_i \log_2(p_i)}{\log_2 N}, \tag{2}$$

$$p_i = \frac{X_i}{\sum_{j=1}^{N} X_j}, \quad \sum_{i=1}^{N} p_i = 1 \tag{3}$$

where X_i is the discrete Fourier Transform of a signal $x_i = x(t_i)$, $t_i = \Delta t \cdot (i-1)$, $i = 1, N$; p_i is the i^{th} frequency's percentage in the whole spectrum, called the probability mass function.

Before processing the Laser or accelerometer signals, a simple normalization is considered, to have comparable evaluations of the *SE*: $x(t) = \frac{s(t)-\bar{s}}{\max(s(t))}$, where $\bar{s}$ is the mean value.

The SE is evaluated on a time history of 525,231 samples with a moving window of 2500 samples, given the temporal width of the EE, the time history is sampled at 25,600 Hz.

Fig. 16a, b, and c shows the *SE* (red line) and the time history (cyan line) for the tests carried out at the lowest energy level. Note that the time histories represent the normalized signals. The base acceleration shows a regular *SE* vs. time, with a maximum of 0.5145, similar to the other signals: top vertical accelerations 0.4000, 0.4001, 0.4012, points 24, 25, 26, respectively; top radial acceleration 0.8624, 0.5907, 0.8494; shell lateral vibration 0.4954.

By increasing the drive level up to 0.05 Vrms, 0.1 Vrms, 0.125 Vrms, and 0.15Vrms (Figs. 17–20), the *SE* continues to be regular, even though at 0.15Vrms some small local increments are visible (their absolute amplitude is still small and are considered below the threshold). At 0.2Vrms Drive (Fig. 21), the *EEs* become evident in the Laser measurements on the shell and the radial vibration of the top mass, now the maxima of *SE* are: base 0.4229; Top vertical 0.3892, 0.3890, 0.3899; Top radial 0.6767, 0.3999, 0.6940; shell 0.6129. Note that, for the radial top mass acceleration and the shell lateral Laser measurements, the *SE* strongly increases; moreover, for the case of the shell, the *SE* vs. time shows a peak in the coincidence of the strongest *EE* at about 5 s.

Similar behaviour of the *SE* is observed for higher energy tests (drives 0.225 and 0.25 Vrms, Figs. 22–23), the Top mass radial signals and the Laser signal give higher *SE*; again, only for the Laser signal, the *SE* is not stationary but presents peaks in correspondence of the *EE*. For the Laser data, the *SE* has a peak of 0.7378 for the event appearing at 3.2 s.

Here the evaluation of the *SE* confirms that, in correspondence with the *EE* there is a local magnification of the Laser signal complexity, i.e. a local maximum of the *SE*; this can be explained by the local spectral analysis, where it has been shown that the spectrum contains several harmonics of the modes of vibration, which are absent at lower levels of excitation. Note that, even though in the radial vibration the peaks are visible, the *SE* does not detect the event, as it maintains its path without peaks. The latter observation allows us to claim that the increment of complexity is generated inside the shell; therefore, even though the phenomenon is recorded by the accelerometers in the top mass, such data do not deliver the information content of the direct measurement on the shell.

4.3. Probability of the temporal distribution of Ghost Hammering

Ghost Hammerings are characterized by transient spikes and exhibit complex temporal patterns. To investigate its probabilistic behaviour over time, this section analyses the temporal distribution of *EEs* at 40 °C and 0.2 V, considering the base and top accelerations as well as the lateral response. Detecting spurious spikes or unrelated events in a random signal usually refers to identifying transients or peaks that do

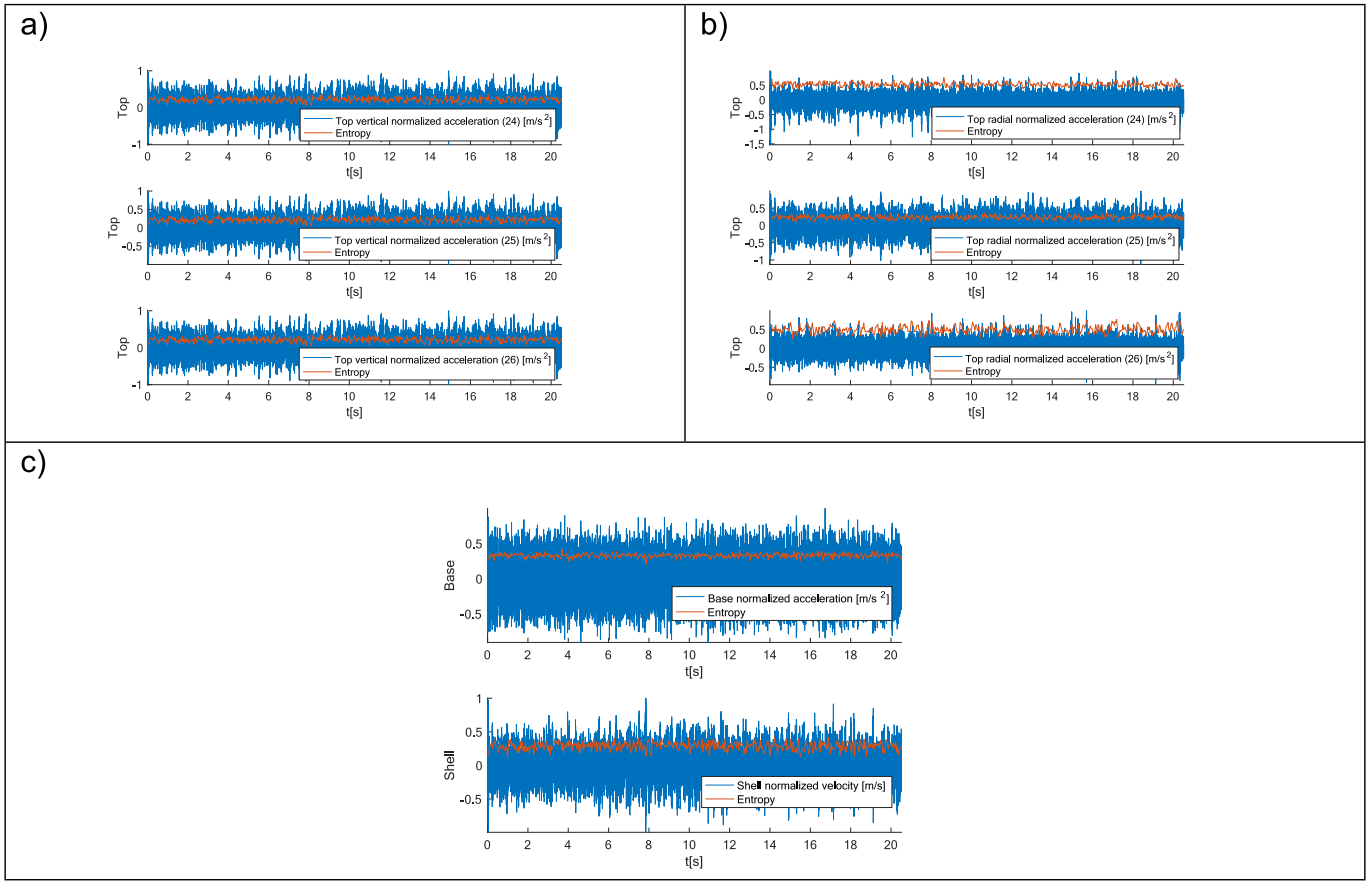

Fig. 18. Entropy of the random signals: Drive 0.1 V, temperature 0 °C.

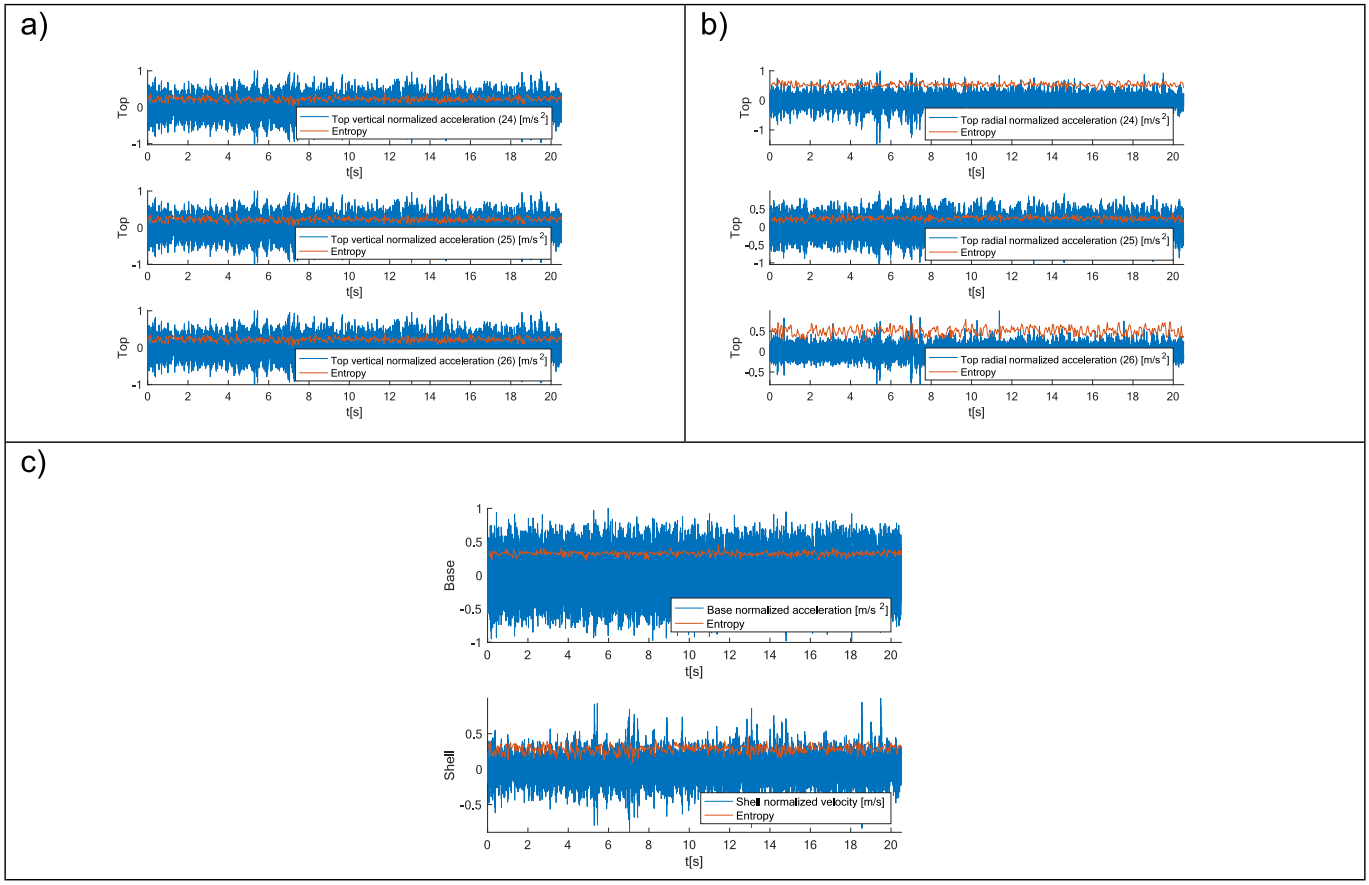

Fig. 19. Entropy of the random signals: Drive 0.125 V, temperature 0 °C.

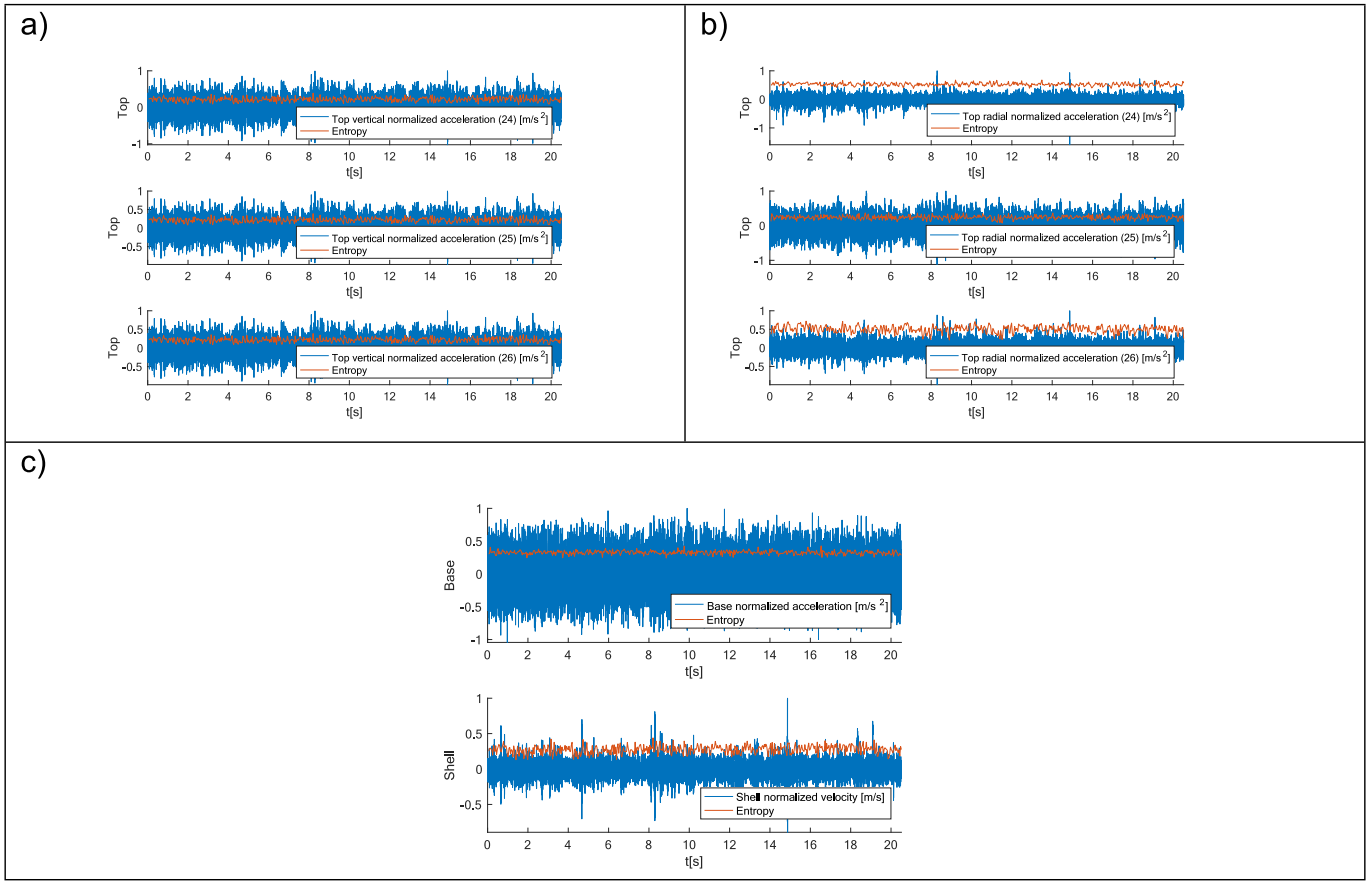

Fig. 20. Entropy of the random signals: Drive 0.15 V, temperature 0 °C.

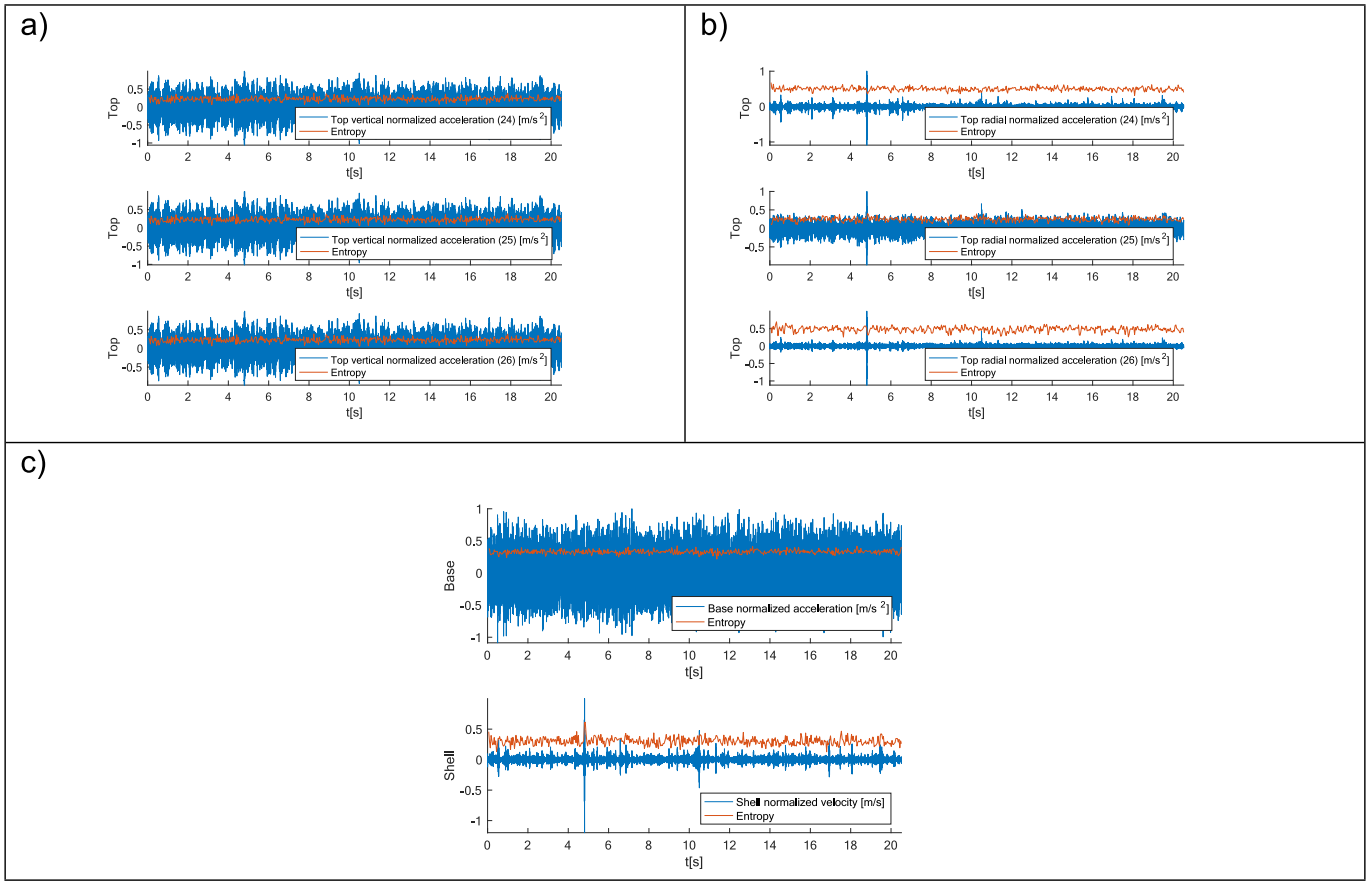

Fig. 21. Entropy of the random signals: Drive 0.2 V, temperature 0 °C.

not correspond to meaningful or expected phenomena and are not part of the actual underlying process. For example, in Neuroscience, detecting spikes in EEG or EMG can be mistaken for movement artifacts or line noise; in mechanical systems, vibrations or impulses might appear due to gear backlash, or loose parts.

For each time history, a threshold level is defined, and all events exceeding this level are identified as *EE*. Values exceeding 20 % and 60 % of the maximum amplitude of the signal are grouped into bins and represented using histogram charts: with a histogram bin of 0.01 s, the first bin will gather all *EE* with a frequency up to 100 Hz, in the second bin all *EE* between 100 Hz and 50 Hz, in the third bin between 50 Hz and 33,3 Hz, etc. Additionally, a parameter referred to as cluster peak—expressed in seconds—defines the minimum time interval required for consecutive peaks to be treated as separate events; only the highest peak within each cluster (i.e., within the cluster peak interval) is retained to avoid counting closely spaced peaks multiple times: if the cluster peak parameter is 0.0005 s all spikes that are more frequent than 2000 Hz are filtered out. The time intervals between these filtered peaks are then computed and visualized through histograms, to capture the underlying temporal distribution: two histogram charts are presented for each time history: the cumulative count of InterSpike Intervals (ISI) and the Wald Probability Distribution Function (PDF).

The Wald distribution, also known as the Inverse Gaussian distribution, is particularly useful for detecting structured yet noisy events over time, that occur in a non-completely random pattern, but that are also influenced by randomness or noise. The Wald distribution consists of two key parameters: μ, mean parameter, and λ, shape parameter. The mean parameter represents the average or expected value of the distribution, in a spike train or ISI context, μ is the expected time between detected spikes, while the shape parameter λ represents the spread or dispersion of the distribution: a higher λ makes the distribution narrower and more peaked, with less variance; a lower λ leads to broader spread, more variability or less correlations in ISIs; it reflects how consistent the spike timing is over time.

Table 5 presents the parameters used in this analysis. Four cases are examined: the first is intended to test the sensitivity of the algorithm for the threshold on the base acceleration, while the second and third illustrate the effects of Ghost Hammering on the occurrence of *EE*. The fourth case also addresses the impact of Ghost Hammering but with a finer temporal bin resolution.

In the first test case, see Table 5, a threshold of 20 % and 60 % has been considered, together with a histogram bin of 0.01 s for cumulative ISIs count and 0.001 s for the Wald PDF; it means that all detected spikes closer than 0.01 s are grouped; moreover, along the time history, the cluster peak parameter has been set to 0.0005 s; it means that, if a series of spikes is closer than 0.0005 s, they are clustered together and only the maximum peak in this interval has been considered.

In the representation of the peak's distribution in the time history of the base acceleration, see Fig. 24, it must be considered that the random signal has been generated in the band frequency of 110 Hz -320 Hz, so the majority of peaks are contained in the first bins.

In Fig. 24c and f, ISI and Wald PDF with thresholds of 20 % and 60 % are shown, respectively, along with the corresponding identified peaks. As expected, with the lower 20 % threshold, more peaks are detected, and their cumulative distributions are primarily concentrated in the first bin (see Fig. 24a and d). This occurs because only spikes with frequencies up to 2000 Hz are considered (using a cluster peak parameter of 0.0005 s), and clustering merges all spikes occurring within 0.01 s (i.e., up to 100 Hz) into the first bin. Conversely, with the higher 60 % threshold, fewer peaks are detected, their distribution appears more fragmented, and their occurrences are less frequent. This is due to fewer peaks exceeding the higher threshold, and when they do, the events are

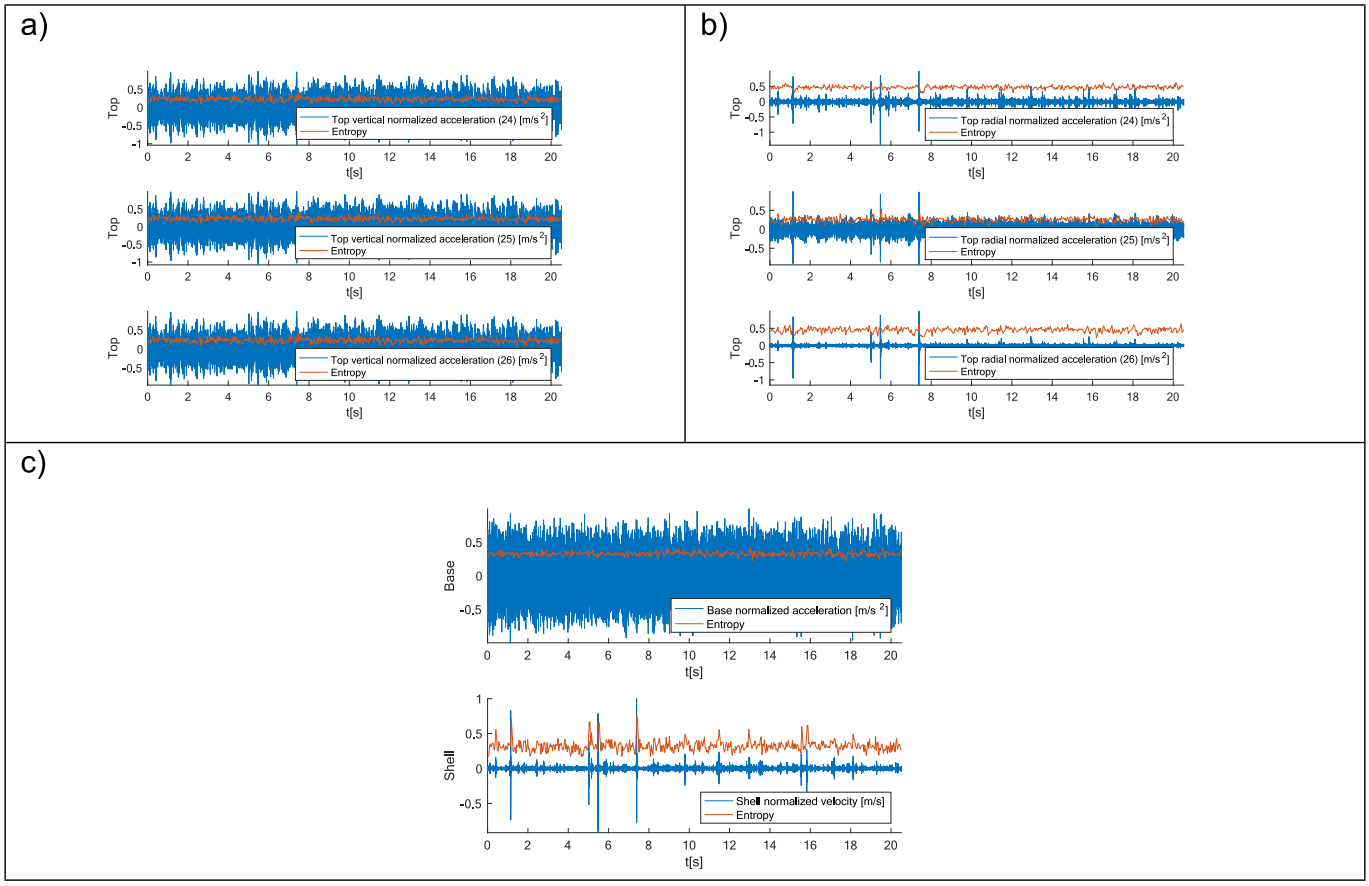

Fig. 22. Entropy of the random signals: Drive 0.225 V, temperature 0 °C.

rarer. The time scale of the cumulative count of InterSpike Intervals (ISIs) extends up to 0.5 s for the 60 % threshold, compared to just 0.04 s for the 20 % case (see Fig. 24a and d).

The Wald probability density function (PDF) for the 20 % threshold (Fig. 24b) indicates that nearly all signal spikes are concentrated around 0.01 s. With the 60 % threshold (Fig. 24e), this concentration is less pronounced. However, the shape parameters of the two PDFs are consistent (0.0210 vs. 0.0196), suggesting that the spikes identified at both thresholds exhibit a similar level of randomness.

In Case 2, the lateral response was analysed; in the first attempt, the same parameters used for the base acceleration analysis were applied, with a threshold set at 20 % of the signal's maximum value (see Fig. 25c). The cumulative count of InterSpike Intervals (ISIs) is primarily concentrated in the first bin (see Fig. 25a). However, the shape parameter is one order of magnitude lower (0.0011706) compared to that of the base acceleration (0.021), indicating that, aside from the initial bin, the spike distribution is more uniform over time. This is further confirmed by the longer timescale of spike occurrences (up to 1.5 s) and the enlargement shown in Fig. 25b, where several bins with low occurrence are present.

The nature of the *GH* spikes is related to a sudden energy transfer to the shell modes at higher frequencies, compared to the excitation's random bandwidth, which primarily excites the axisymmetric mode at lower frequencies. This energy transfer generates a burst that produces an oscillating series of high-frequency oscillations. To better identify this phenomenon, a higher cluster peak parameter of 0.05 s was considered.

To enhance the uniform distribution of the spikes in the lateral response of the shell, the cluster parameter has been settled to 0.05 s, see Fig. 26; the results clearly show the uniform occurrence of the spikes, the external random forcing, or stochastic forcing, dominates the dynamics, flattening any internal structure, so the oscillators do not settle into synchronized rhythms, in the recurrence of the spikes that occur almost randomly in time.

4.4. Recurrence Quantification Analysis (RQA)

To further investigate the underlying dynamics of the lateral response and to quantify the structure of the ghost hammering phenomena, Recurrence Quantification Analysis (RQA), see Ref. [65], was employed. RQA is a nonlinear time-series analysis method that reveals the recurrence patterns of a dynamical system in its reconstructed phase space and allows for the extraction of quantitative information from time histories. This approach is particularly suitable for detecting subtle transitions, intermittent behaviour, or hidden periodicities in complex signals, especially when traditional linear metrics are insufficient. In the context of the lateral response, RQA enables the characterization of recurrent patterns associated with high-frequency bursts and clustered spike activity.

The RQA has been performed considering 0.4 s of time history, sampled at 25600 Hz, at 40 °C and 0.2 Vrms; both from base acceleration and lateral velocity the time window is centred at one of the *EE* locations, see Figs. 27a and 29a: 10240 samples from 6.15 s to 6.55 s are considered here.

In Fig. 27a, the time history shows, as expected, the general random behaviour of the forcing load. In Fig. 27b, the PSD confirms that the bandwidth of the base acceleration, highlighted with a red rectangle, is between 110 Hz and 320 Hz; it can be noted a peak at 259 Hz that is due to the resonance of the axisymmetric mode, that interacts with the base and detected from the base accelerometer. Nevertheless, the broad behaviour is random, which is strongly verified by the recurrence plot (RP), in Fig. 28.

The analysis that generates the RP has been made considering 100

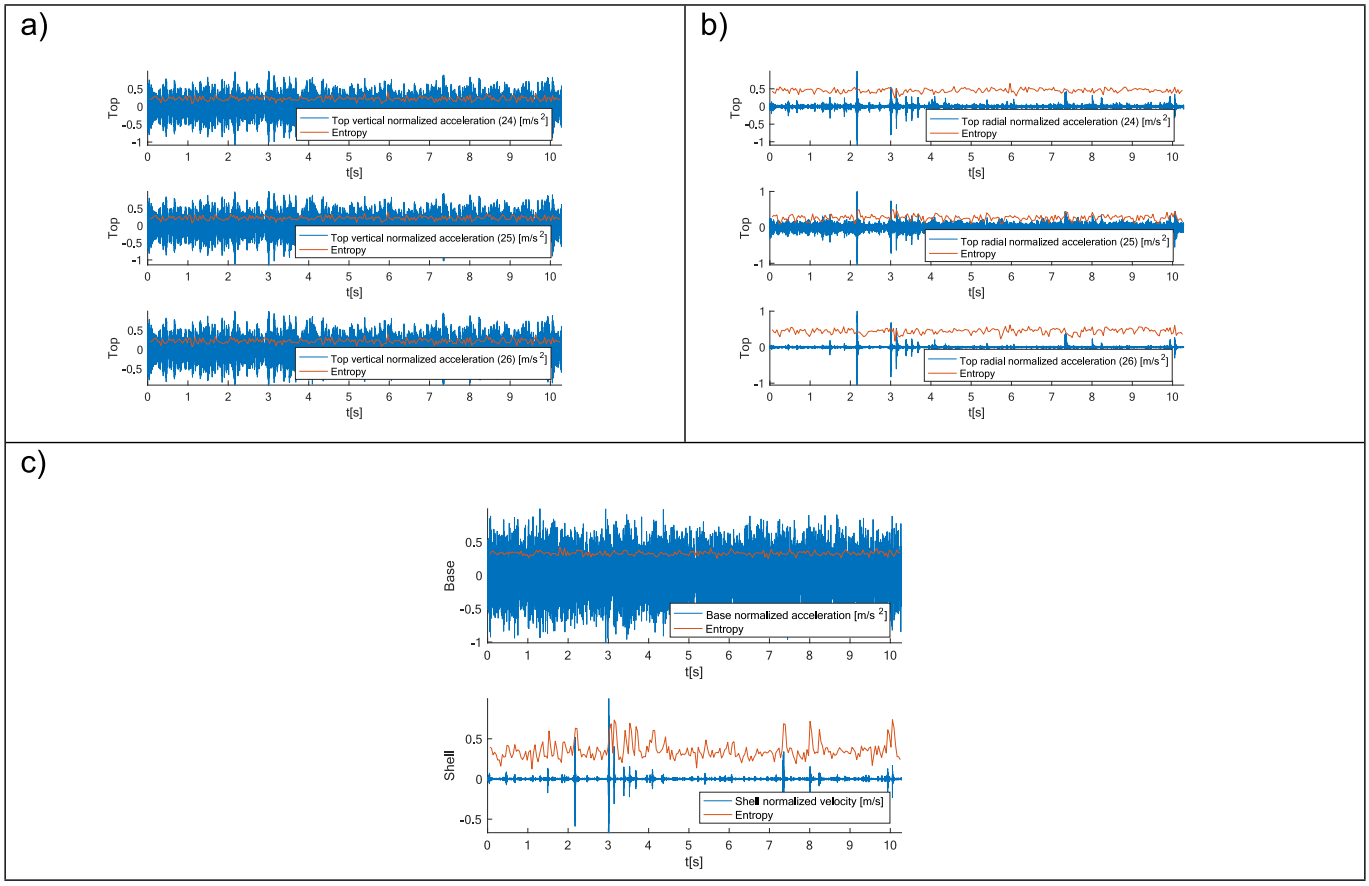

Fig. 23. Entropy of the random signals: Drive 0.25 V, temperature 0 °C.

Table 5
Parameter for event identification.

Test case	Signal	Peak threshold in % of the maximum value	Cluster peak [s]	Histogram bin [s]
1	Base acceleration	20	0.0005	0.01–0.001
	Base acceleration	60	0.0005	0.01–0.001
2	Lateral response (shell)	20	0.0005	0.01–0.001
	Lateral response (shell)	20	0.05	0.01–0.001

bins, a delay of 28 samples, and an embedding dimension of 3: the mutual information test has been used to determine the time delay, find the first minimum at 28 samples; the false nearest neighbours' technique has been applied to determine the embedding dimension. In Fig. 28a the overall behaviour is presented: the main diagonal line, called also the Line Of Identity (LOI) can be detected, this line is always present because each state is recurrent with itself and appears in the plot as a solid diagonal line from top-left to bottom-right; irregular spaced vertical and horizontal lines are present in the coloured RP and shows that the system remains in the same state for some time, ongoing random behaviour with consistent statistical properties over time, with long vertical lines that represent trapping in a specific state. This perduration of stochastic random dynamics is visible in the black and white RP, Fig. 28b, where the LOI is strongly evident and scattered dots with no clear structure are present. Looking closer at the enlarged image between samples 2400 and 3600, Fig. 28c, and 6000 and 7200 samples, Fig. 28d, diagonal structures can be noted, parallel to the LOI, spaced by 99 samples, one to each other. These short diagonal structures point out the presence of a sort of periodicity at 258 Hz (consider the sampling frequency of 25,600 Hz divided by 99, the number of samples), that can be related to the peak in the PSD: this shows that this harmonic, due to axisymmetric mode response, has a detectable influence in the base acceleration signal. It is important to note that, those structures do not represent a deterministic behaviour because the shapes are not equal to defined straight lines but are fluid and evolving structures along the time domain.

In the lateral response of the shell, the behaviour is strongly different, this can be seen from the time history, see Fig. 29a, where in the enlarged view of the EE the presence of regular oscillations is evident, the distribution is not random but concentrated in specific frequencies as shown by the PSD, see Fig. 29b; in particular, the peak at 256 Hz, can be related to mode 4 (254 Hz), see Table 4, the peaks at 771 Hz and 784 Hz are related to modes 7 (786 Hz) and 8 (805 Hz).

A 10240 samples time history is processed, with a partition of 100 samples, the embedding delay is 9 and the embedding dimension is 3. The RP, Fig. 30a, shows a more regular structure with a stochastic fragmentation, but with a strong deterministic character: a wide portion of the RP is involved with vertical and horizontal lines between samples 4000 and 6000, which show that the dynamics, in this case, remain in the same state for a certain time and the shell response is trapped in a specific state of intermittency; this is better enhanced in the black and white RP, Fig. 30b, where scattered points are not completely placed in unstructured aleatory locations, but they are more organized along diagonals parallel to the LOI; such long diagonals indicate an evolution in different parts of the time series: strongly regular or governed by deterministic patterns.

By analysing the time history between samples 0 and 600, Fig. 30c, the presence of diagonal lines is clear, the spacing is 100 and 33 samples, corresponding to periodicity of 255 Hz and 777 Hz. The spaced parallel diagonal lines are longer than in the previous case, and more regular,

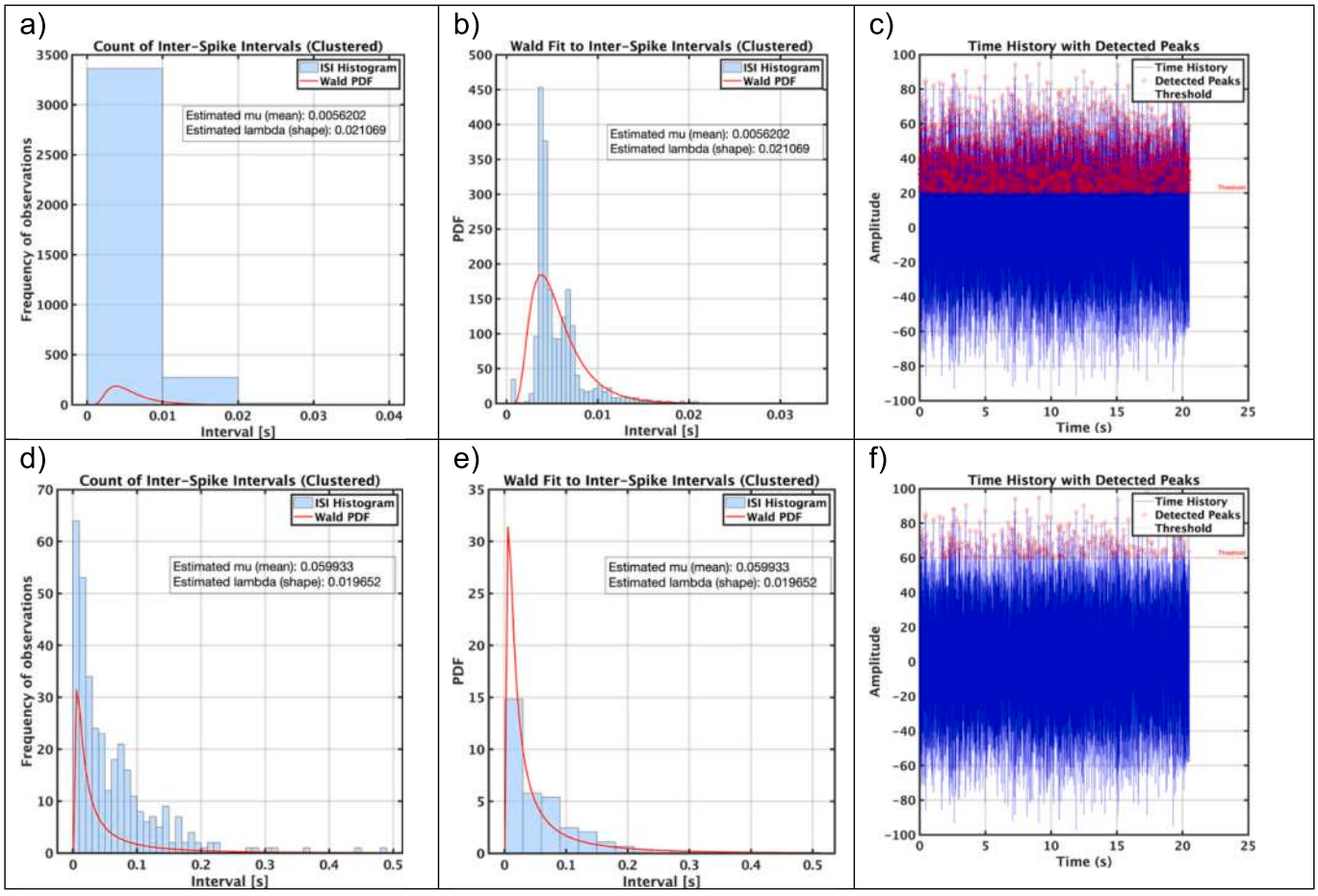

Fig. 24. Case 1 probability distribution of spikes in time history, base acceleration.

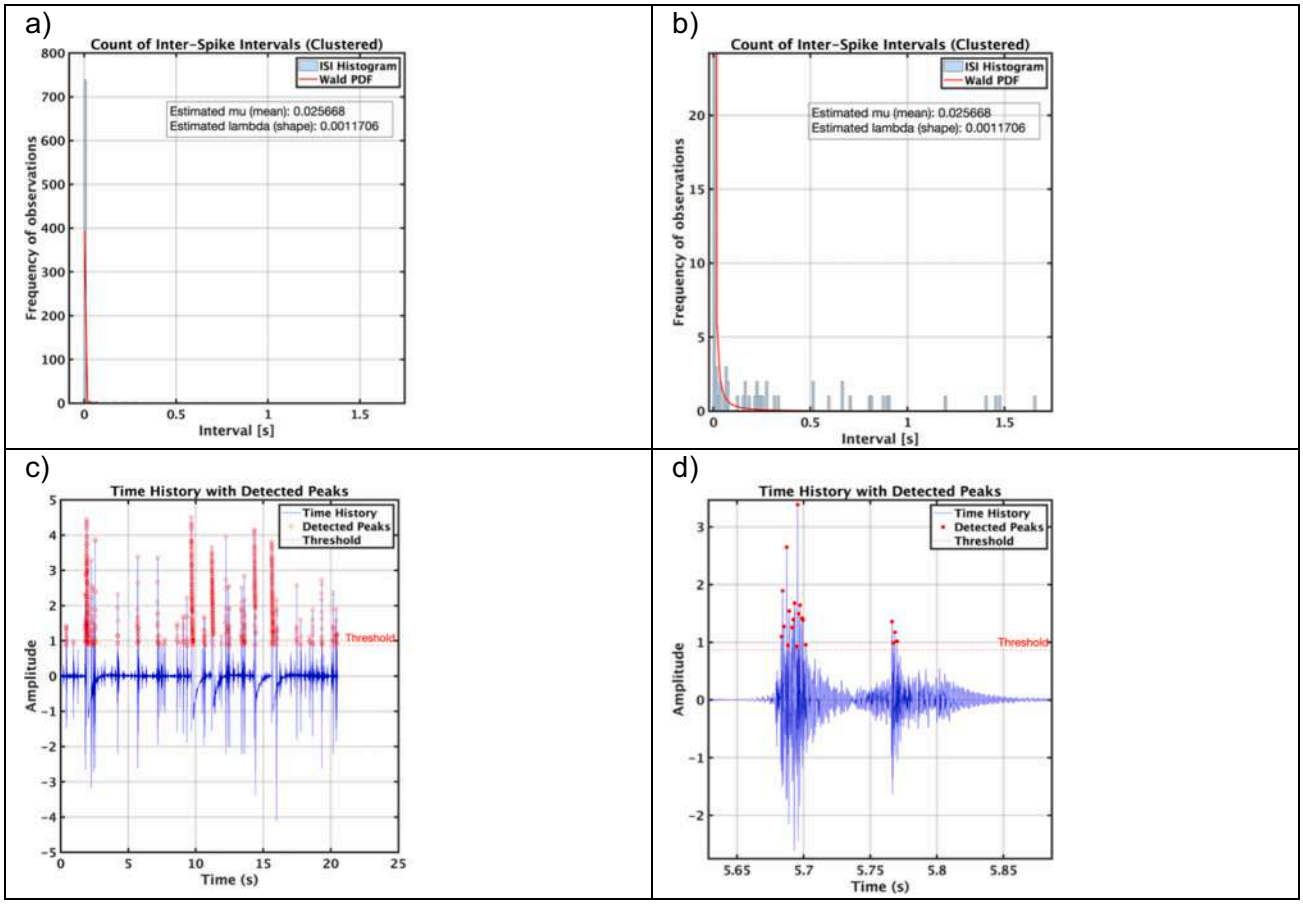

Fig. 25. Case 2 probability distribution of spikes in time history, cluster peak parameter = 0.0005 s, lateral shell vibration.

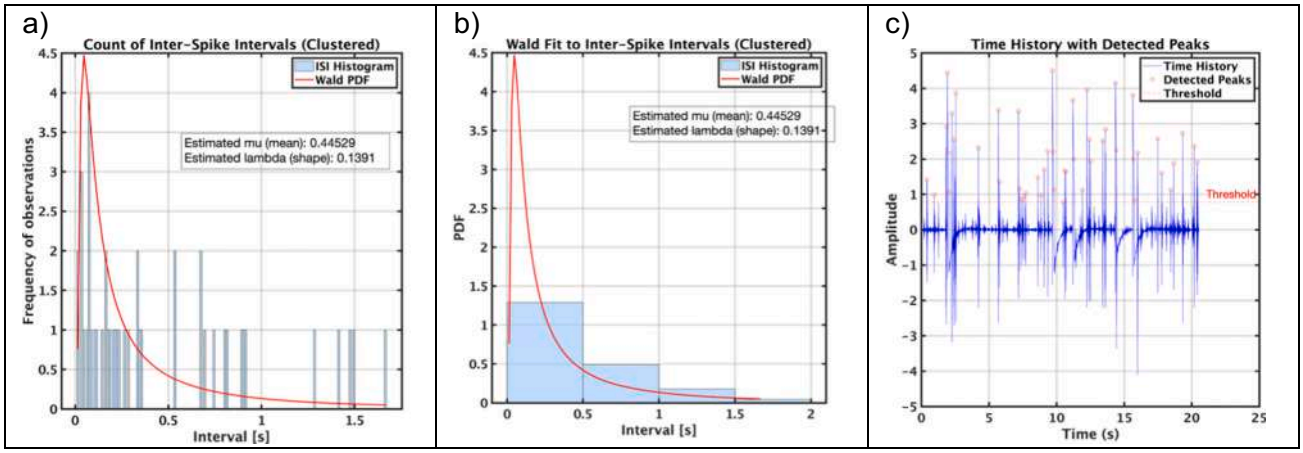

Fig. 26. Case 2 probability distribution of spikes in time history, cluster peak parameter = 0.05 s, lateral shell vibration.

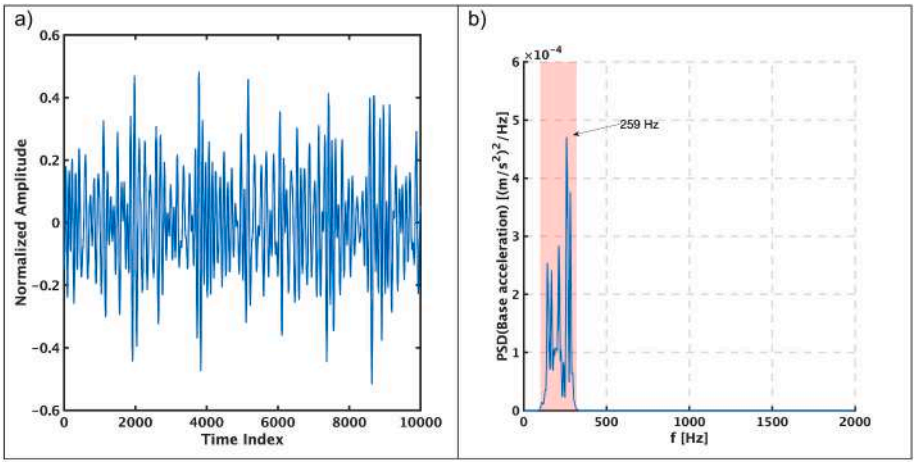

Fig. 27. Base acceleration considering 10,000 samples: a) time history, b) PSD.

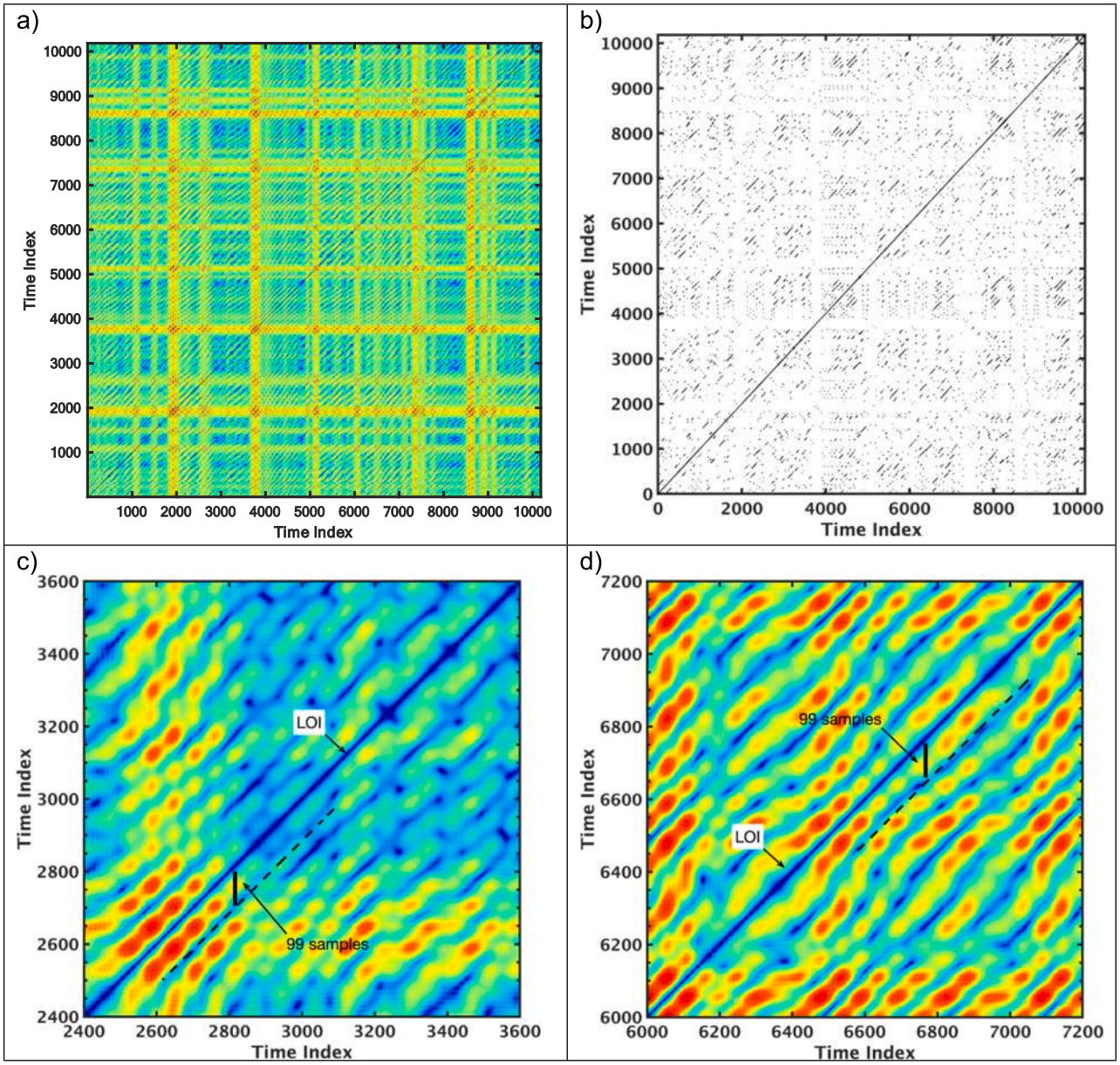

Fig. 28. Recurrence plot of base acceleration: a) coloured overall plot, b) black and white overall plot, c) detail between 2400 and 3600 samples, d) detail between 6000 and 7200 samples.

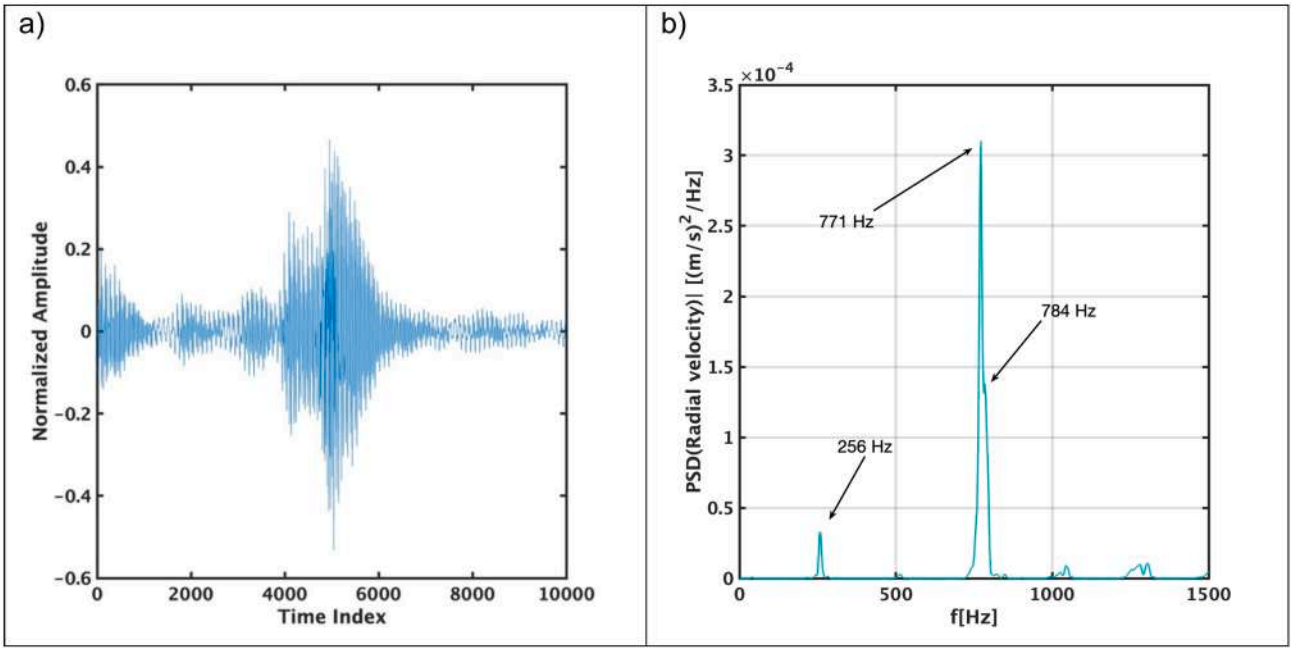

Fig. 29. Lateral velocity considering 10,000 samples: a) time history, b) PSD.

even if not continuous, highlighting the effect in the response of the shell dynamics; moreover, in the central part of the RP, see Fig. 30d, it can be noted a transient of periodicity from 255 Hz to 777 Hz, moving along the LOI from the bottom left to the top right corner, the intensity of the spaced segment vary from 100 samples to 33 samples highlighting this behaviour.

4.5. Approximate Entropy (AE)

To quantify the regularity of the nonlinear time series, the Approximate Entropy (AE) is now considered, such an approach is based on the embedding technique, and the time delay and embedding dimension are the same as in the previous section. The Approximate Entropy is a complementary concept with respect to the Spectral Entropy used in the previous section, *AE* and SE quantify the complexity or irregularity of signals; however, their approach is different from mathematical and conceptual perspectives: the *SE* is a measure of the disorder or randomness of a signal based on its frequency content and applies the Shannon entropy to the Power Spectral Density of a signal; conversely, AE quantifies the regularity and unpredictability of fluctuations in a time series, it measures the likelihood that patterns repeat over time: lower *AE* indicates highly regular or predictable signal, as constant or periodic signals, while higher *AE* points out irregular or unpredictable signal, as chaotic or random signal. In the present time histories, for the base acceleration, the approximate entropy is 0.9504, while for the lateral velocity is 0.8336.

Besides the approximate entropy, to better characterize the behaviour of the analysed time series, RQA metrics have also been computed. RQA provides a set of quantitative measures that extend beyond the visual impression offered by RPs, enabling a detailed assessment of the complexity inherent in the small-scale structures of the RP. These metrics are based on the density of recurrence points and the distribution of diagonal and vertical line structures. By calculating them over small, moving windows (sub-matrices) along the line of identity, the time-dependent evolution of the system's dynamics can be effectively captured., i.e. the Recurrence Rate (RR), using a threshold of 1 %, as shown in Table 6. It can be noted that the *RR* is low in both cases, but a little higher in the radial shell vibration: such values are consistent, because random signals have, in general, low RR, while periodic signals have low/moderate RR. Determinism (DET) reaches 84.76 % in the radial shell vibration, with respect to base acceleration (53 %), the Laminarity (LAM), which is a feature to quantify the intermittency, reaches 70.45 % compared with the base that is only 13.56 %. Moreover, the AE is higher in the radial shell vibration, as mentioned before, in RQA. The Shannon entropy (ENTR) typically measures the diversity of diagonal line lengths in the recurrence plot and not the signal's randomness directly. ENTR reflects how complex or varied the system's evolution patterns are over time, and a random signal is unpredictable, but also structureless, while the deterministic component in the response of the lateral shell vibration, with oscillating spikes, is predictably unpredictable, and it shows complex patterns of recurrence.

5. Conclusions

This study provides compelling experimental evidence of a novel nonlinear dynamic phenomenon, termed “Ghost Hammering,” in a circular cylindrical shell subjected to narrowband random excitation. Unlike the responses predicted by linear models, the observed behaviour involves irregular, high-amplitude, and oscillatory spikes that resemble transient impacts but occur without any external impulsive force. These Extreme Events are found to be driven by stochastic excitation and result from interactions between modes; specifically, between the axisymmetric mode, which is directly excited by base motion, and higher-order shell modes. Moreover, the stochastic excitation occasionally reaches levels that are sufficient to induce shell buckling. This can give rise to a temporary loss of equilibrium stability and the emergence of multiple equilibria. Detailed spectral and temporal analyses, including entropy evaluation and recurrence quantification, reveal that the spikes are composed of coherent oscillations with spectral content matching the natural frequencies of the structure, confirming a deterministic component underlying the random excitation. The findings demonstrate a critical dependence on excitation energy and temperature, with the damping ratio emerging as a key factor influencing the threshold for spike generation. The phenomenon shows striking similarities with stochastic bursting and spiking events in neuronal systems and other complex nonlinear dynamical contexts, though the oscillatory nature of the spikes in Ghost Hammering sets it apart. Traditional theories of stochastic resonance do not fully explain the observed dynamics,

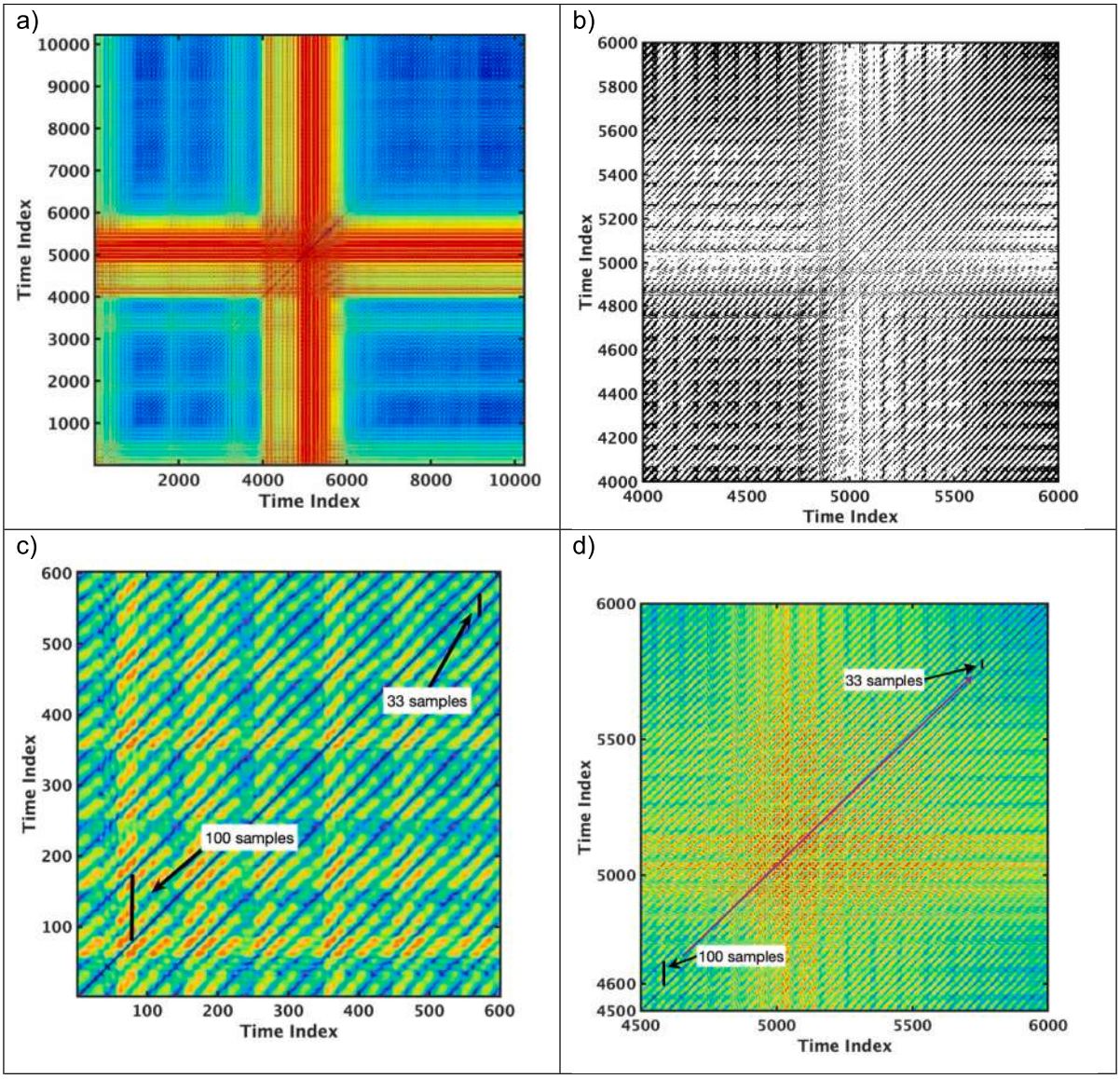

Fig. 30. Recurrence plot of lateral velocity: a) coloured overall plot, b) black and white overall plot, c) initial detail RP, d) central detail of RP.

Table 6
Recurrence Quantification Analysis (RQA) metrics.

Metric	Interpretation	Base acceleration	Radial velocity
Recurrence rate (RR)	% of recurrence points in the plot. High RR = more repetitive system behaviour.	0.022	0.613
Determinism (DET)	% of recurrence points forming diagonal lines. High DET = predictable, deterministic system.	53.79	84.76
Max diagonal length (Lmax)	Longest diagonal line. The inverse is related to the system's divergence or Lyapunov exponent.	109	2075
Entropy (ENTR)	Shannon entropy of diagonal line lengths. High ENTR = more complexity in system dynamics.	2.77	3.22
Laminarity (LAM)	% of recurrence points forming vertical lines. High LAM = laminar states or intermittency.	13.56	70.45
Trapping time (TT)	Average length of vertical lines. Related to how long the system stays in a specific state.	3.58	4.50

suggesting a need for new models or adaptations of existing ones—such as extensions of Langevin or FitzHugh–Nagumo systems—to structural mechanics. This work opens promising directions for future research in understanding noise-induced phenomena in mechanical systems and highlights the importance of considering nonlinearities and random effects in the design and analysis of advanced structural components. The full dataset is available at: doi:10.17632/pj3824wfpr.2 [67].

CRediT authorship contribution statement

Francesco Pellicano: Writing – review & editing, Writing – original draft, Visualization, Validation, Supervision, Software, Resources, Project administration, Methodology, Investigation, Funding acquisition, Formal analysis, Data curation, Conceptualization. **Antonio Zippo:** Writing – review & editing, Writing – original draft, Visualization, Validation, Supervision, Software, Resources, Project administration, Methodology, Investigation, Funding acquisition, Formal analysis, Data curation, Conceptualization.

Declaration of competing interest

The authors declare the following financial interests/personal relationships which may be considered as potential competing interests: Francesco Pellicano reports financial support was provided by NATO. Francesco Pellicano is Editorial Board Member of Chaos, Solitons & Fractals. The other author declares that he has no known competing financial interests or personal relationships that could have appeared to influence the work reported in this paper.

Acknowledgments

The authors acknowledge NATO SPS program, project G6176 “Composite Metamaterials for Aerospace Structures -- CoMetA” for the financial support.

Data availability

Data is available on Mendeley: https://doi.org/10.17632/pj3824wfpr.2

References

[1] Bendat JS, Piersol AG. Random data: analysis and measurement procedures. In: Wiley series in probability and statistics. 3rd ed. 2010. https://doi.org/10.1002/9781118032428.
[2] Caughey TK. Nonlinear theory of random vibrations. In: Advances in applied mechanics. vol. 11. Elsevier; 1971. p. 209–53. https://doi.org/10.1016/S0065-2156(08)70343-0.
[3] Roberts JB, Spanos PD. Random vibration and statistical linearization. John Wiley & Sons; 1999.
[4] Spanos PD, Donley MG. Equivalent statistical quadratization for nonlinear systems. J Eng Mech 1991;117(6):1289–310.
[5] Benzi R, Sutera A, Vulpiani A. The mechanism of stochastic resonance. J Phys A Math Gen 1981;14:L453–7.
[6] Graham R. Forward Hopf bifurcation with multiplicative gaussian white noise: exact Fokker-Planck solution. Physics Letters A 1980;80(5–6):351–3. https://doi.org/10.1016/0375-9601(80)90765-3.
[7] Gammaitoni L, Hänggi P, Jung P, Marchesoni F. Stochastic resonance. Rev Mod Phys 1998;70(1):223–87.
[8] Gao JB, Hwang SK, Liu JM. When can noise induce chaos? Phys Rev Lett 1999;82(6):1132–5.
[9] Feng ZH, Hu HY. Largest Lyapunov exponent and almost certain stability analysis of slender beams under a large linear motion basement subjected to narrowband parametric excitation. J Sound Vib 2002;257(4):733–52.
[10] Young TH, Gau CY. Dynamic stability of spinning pre-twisted beams subjected to axial random forces. J Sound Vib 2003;268(1):149–65. https://doi.org/10.1016/S0022-460X(02)01490-6.
[11] Li J, Xu W, Ren Z, Lei Y. Maximal Lyapunov exponent and almost-sure stability for stochastic Mathieu–Duffing systems. J Sound Vib 2005;286(1–2):395–402. https://doi.org/10.1016/j.jsv.2004.11.029.
[12] Muratova CB, Vanden-Eijndenb E, W. E. Self-induced stochastic resonance in excitable systems. Physica D 2005;210:227–40. https://doi.org/10.1016/j.physd.2005.07.014.
[13] Dobson I, Carreras BA, Lynch VE, Newman DE. Complex systems analysis of series of blackouts: cascading failure, critical points, and self-organization. Chaos: An Interdisciplinary Journal of Nonlinear Science 2007;17(2):026103. https://doi.org/10.1063/1.2737822.
[14] Bonatto C, Feyereisen M, Barland S, Giudici M, Masoller C, Rios Leite JR, et al. Deterministic optical rogue waves. Phys Rev Lett 2011;107:053901.
[15] Brouwers JJH. Asymptotic solutions for Mathieu instability under random parametric excitation and nonlinear damping. Physica D: Nonlinear Phenomena 2011;240(12):990–1000. https://doi.org/10.1016/j.physd.2011.02.009.
[16] Tantet A, Chekroun MD, Dijkstra HA, et al. Ruelle-Pollicott resonances of stochastic systems in reduced state space. Part II: stochastic Hopf bifurcation. Journal of Statistical Physics 2020;179:1403–48. https://doi.org/10.1007/s10955-020-02526-y.
[17] Zhu H, Geng G, Yu Y, Xu L. Probabilistic analysis on parametric random vibration of a marine riser excited by correlated Gaussian white noises. International Journal of Non-Linear Mechanics 2020;126:103578. https://doi.org/10.1016/j.ijnonlinmec.2020.103578.
[18] Ramakrishnan S, Edlund C. Stochastic stability of a piezoelectric vibration energy harvester under a parametric excitation and noise-induced stabilization. Mechanical Systems and Signal Processing 2020;140:106566. https://doi.org/10.1016/j.ymssp.2019.106566.
[19] Kuptsova EV. Van der pol oscillator under random noise. J Appl Ind Math 2022;16:449–59. https://doi.org/10.1134/S1990478922030097.
[20] Qian J, Chen L. Stochastic P-bifurcation analysis of a novel type of unilateral vibro-impact vibration system. Chaos, Solitons & Fractals 2021;149:111112. https://doi.org/10.1016/j.chaos.2021.111112.
[21] Wang D, Pei H, Xu W, Yao J, Shi J, Kurths J. Resonance characteristics of stochastic dual Duffing oscillators with coupled APHC. J Sound Vib 2021;498:115981. https://doi.org/10.1016/j.jsv.2021.115981.
[22] Yang K, Abdelkefi A, Li X, Mao Y, Dai L, Wang J. Stochastic analysis of a galloping-random wind energy harvesting performance on a buoy platform. Energ Conver Manage 2021;238:114174. https://doi.org/10.1016/j.enconman.2021.114174.
[23] Yu Q, Liu X. Self-induced stochastic resonance in an excitable potential well. Physics Letters A 2021;410:127520. https://doi.org/10.1016/j.physleta.2021.127520.
[24] Bashkirtseva I, Slepukhina E. Variability of complex oscillatory regimes in the stochastic model of cold-flame combustion of a hydrocarbon mixture. Phil Trans R Soc A 2022;380:20200314. https://doi.org/10.1098/rsta.2020.0314.
[25] Ramakrishnan S, Singh AK. Stochastic dynamics of a nonlinear vibration energy harvester subjected to a combined parametric and external random excitation: the distinct cases of Itô and Stratonovich stochastic integration. International Journal of Non-Linear Mechanics 2024;162:104700. https://doi.org/10.1016/j.ijnonlinmec.2024.104700.
[26] Zhang R, Meng L, Yuan GX, Wang H. Collective dynamics of coupled oscillators with damping fluctuation in small-world complex networks. Chinese Journal of Physics 2024;92:1628–40. https://doi.org/10.1016/j.cjph.2024.11.026.
[27] Fitzhugh R. Impulses and physiological states in theoretical models of nerve membrane. Biophys J 1961;1:445–66.
[28] Baltanáis JR, Casado JM. Bursting behaviour of the FitzHugh-Nagumo neuron model subject to quasi-monochromatic noise. Physica D 1998;122:231–40.
[29] Muratov CB, Vanden-Eijnden E. Noise-induced mixed-mode oscillations in a relaxation oscillator near the onset of a limit cycle. Chaos: An Interdisciplinary

Journal of Nonlinear Science 2008;18(1):015111. https://doi.org/10.1063/1.2779852.
[30] Faisal A, Selen L, Wolpert D. Noise in the nervous system. Nat Rev Neurosci 2008; 9:292–303. https://doi.org/10.1038/nrn2258.
[31] Channell P, Fuwape I, Neiman AB, Shilnikov AL. Variability of bursting patterns in a neuron model in the presence of noise. J Comput Neurosci 2009;27:527–42. https://doi.org/10.1007/s10827-009-0167-1.
[32] Tsimring LS. Noise in biology. Rep Prog Phys 2014;77:026601. https://doi.org/10.1088/0034-4885/77/2/026601.
[33] Sgro AE, Schwab DJ, Noorbakhsh J, Mestler T, Mehta P, Gregor T. From intracellular signaling to population oscillations: bridging size- and time-scales in collective behavior. Mol Syst Biol 2015;11(1):1744–4292. https://doi.org/10.15252/msb.20145352.
[34] Gupta P, Balasubramaniam N, Chang H-Y, Tseng F-G, Santra TS. A single-neuron: current trends and future prospects. Cells 2020;9:1528. https://doi.org/10.3390/cells9061528.
[35] Ryashko L, Slepukhina E. Noise-induced toroidal excitability in neuron model. Communications in Nonlinear Science and Numerical Simulation 2020;82:105071. https://doi.org/10.1016/j.cnsns.2019.105071.
[36] Manchein C, Santana L, da Silva RM, Beims MW. Noise-induced stabilization of the FitzHugh–Nagumo neuron dynamics: multistability and transient chaos. Chaos: An Interdisciplinary Journal of Nonlinear Science 2022;32(8). https://doi.org/10.1063/5.0086994.
[37] Nkounga IBT, Xia Y, Yanchuk S, Yamapi R, Kurths J. Generalized FitzHugh–Nagumo model with tristable dynamics: deterministic and stochastic bifurcations. Chaos Solitons Fractals 2023;175(1):114020. https://doi.org/10.1016/j.chaos.2023.114020.
[38] López J, Coccolo M, Capeáns R, Sanjuán MAF. Controlling the bursting size in the two-dimensional Rulkov model. Communications in Nonlinear Science and Numerical Simulation 2023;120:107184. https://doi.org/10.1016/j.cnsns.2023.107184.
[39] Wu Y, Sun Z, Zhao N. Resonance dynamics in multilayer neural networks subjected to electromagnetic induction. Communications in Nonlinear Science and Numerical Simulation 2025;143:108575. https://doi.org/10.1016/j.cnsns.2024.108575.
[40] Vijay SD, Thamilmaran K, Ahamed AI. Superextreme spiking oscillations and multistability in a memristor-based Hindmarsh–Rose neuron model. Nonlinear Dyn 2023;111:789–99. https://doi.org/10.1007/s11071-022-07850-4.
[41] Hariharan S, Suresh R, Chandrasekar VK. Noise-induced extreme events in integer and fractional-order memristive Hindmarsh–Rose neuron models: a comprehensive study. Eur Phys J Plus 2024;139:292. https://doi.org/10.1140/epjp/s13360-024-05059-5.
[42] Cebrían-Lacasa D, Parra-Rivas P, Ruiz-Reynés D, Gelens L. Six decades of the FitzHugh-Nagumo model: a guide through its spatio-temporal dynamics and influence across disciplines. Phys Rep 2024:1–39.
[43] Hariharan S, Suresh R, Chandrasekar VK. Noise-induced extreme events in single Fitzhugh–Nagumo oscillator. Chaos Solitons Fractals 2025;192:116077. https://doi.org/10.1016/j.chaos.2025.116077.
[44] Pellicano F, Barbieri M, Zippo A, Strozzi M. Experiments on shells under base excitation. J Sound Vib 2016;369:209–27. https://doi.org/10.1016/j.jsv.2015.12.033. ISSN: 0022-460X.
[45] Pellicano F, Barbieri M. Complex dynamics of circular cylindrical shells. Int International Journal of Non-Linear Mechanics 2014;65:196–212. https://doi.org/10.1016/j.ijnonlinmec.2014.05.006.
[46] Strozzi M, Smirnov VV, Manevitch LI, Milani M, Pellicano F. Nonlinear vibrations and energy exchange of single-walled carbon nanotubes. Circumferential flexural modes. J Sound Vib 2016;381:156–78. https://doi.org/10.1016/j.jsv.2016.06.013.
[47] Zippo A, Barbieri M, Iarriccio G, Pellicano F. Nonlinear vibrations of circular cylindrical shells with thermal effects: an experimental study. Nonlinear Dynamics 2020;99(1):373–91. https://doi.org/10.1007/s11071-018-04753-1.
[48] Iarriccio G, Zippo A, Pellicano F, Barbieri M. Resonances and nonlinear vibrations of circular cylindrical shells, effects of thermal gradients. Proc IMechE Part C J Mech Eng Sci 2021;235(20):4818–32. https://doi.org/10.1177/0954406220907616.
[49] Zippo A, Iarriccio G, Bergamini L, Colombini E, Veronesi P, Pellicano F. Fluid-structure interaction of a thin cylindrical shell filled with a non-newtonian fluid. Journal of Fluids and Structures 2023;117:103829. https://doi.org/10.1016/j.jfluidstructs.2022.103829.
[50] Zippo A, Iarriccio G, Pellicano F. Synchronicity phenomena in circular cylindrical shells under random excitation. Advanced Structured Materials 2021;157:127–57. https://doi.org/10.1007/978-3-030-75890-5_8.
[51] Pellicano F. Vibrations of circular cylindrical shells: theory and experiments. J Sound Vib 2007;303:154–70. https://doi.org/10.1016/j.jsv.2007.01.022.
[52] Yamaki N. Elastic stability of circular cylindrical shells. Amsterdam, The Netherlands: Elsevier Printing; 1984.
[53] Bushnell D. Buckling of shells—pitfall for designers. AIAA Journal 1981;19(9):1183–226.
[54] Pellicano F. Dynamic stability and sensitivity to geometric imperfections of strongly compressed circular cylindrical shells under dynamic axial loads. Commun Nonlinear Sci Numer Simul 2009;14:3449–62. https://doi.org/10.1016/j.cnsns.2009.01.018.
[55] Soedel W. Vibrations of shells and plates. New York: Marcel Dekker Inc.; 1993.
[56] Pellicano F. Dynamic instability of a circular cylindrical shell carrying a top mass under seismic excitation: experiments and theory. Int J of Solids and Structures 2011;48:408–27.
[57] Kolmogorov AN. Doki Akad Nauk SSSR 1958;119:861–4.
[58] Pincus SM. Approximate entropy as a measure of system complexity. Proc Natl Acad Sci U S A 1991;88:2297–301.
[59] Gibson JD. What is the interpretation of spectral entropy?. In: Proceedings of 1994 IEEE International Symposium on Information Theory, Trondheim, Norway; 1994. p. 440. https://doi.org/10.1109/ISIT.1994.395055.
[60] Pan YN, Chen J, Li XL. Spectral entropy: a complementary index for rolling element bearing performance degradation assessment. Proc Inst Mech Eng C J Mech Eng Sci 2009;223(5):1223–31.
[61] Sharma V, Parey A. A review of gear fault diagnosis using various condition indicators. Procedia Engineering 2016;144:253–63.
[62] Shen J, Hung J, Lee L. Robust entropy-based endpoint detection for speech recognition in Noisy environments. In: ICSLP 98; November 1998.
[63] Vakkuri A, Yli-Hankala A, Talja P, Mustola S, Tolvanen-Laakso H, Sampson T, et al. Time-frequency balanced spectral entropy as a measure of anesthetic drug effect in central nervous system during sevoflurane, propofol, and thiopental anesthesia. Acta Anaesthesiol Scand 2004;48(2):145–53.
[64] Misra H, Ikbal S, Bourlard H, Hermansky H. Spectral entropy based feature for robust ASR. In: 2004 IEEE International Conference on Acoustics, Speech, and Signal Processing; 2004. I–193. https://doi.org/10.1109/ICASSP.2004.1325955.
[65] Marwan Norbert, Romano M Carmen, Thiel Marco, Kurths Jürgen. Recurrence plots for the analysis of complex systems. Phys Rep 2007;438(5–6):237–329. https://doi.org/10.1016/j.physrep.2006.11.001.
[66] Ostojic S. Interspike interval distributions of spiking neurons driven by fluctuating inputs. J Neurophysiol Jul 2011;106(1):361–73. https://doi.org/10.1152/jn.00830.2010 [Epub 2011 Apr 27. PMID: 21525364].
[67] Zippo A, Pellicano F. Experimental dataset on ghost hammering phenomena in nonlinear shell structures under stochastic excitation. Mendeley Data 2025;V2. https://doi.org/10.17632/pj3824wfpr.2.